Key Points:
- The physical structure and microphysical properties of a summer austral atmospheric river are described
- Ice particle concentrations increased to >100 L^{-1} in the zone from $-8°C$ to $-4°C$, consistent with secondary ice formation
- Ice particles falling from the tropical-sourced moisture stream aloft trigger coalescence below the 0°C isotherm

Correspondence to:
R. M. Rauber,
r-rauber@illinois.edu

Author Contributions:
Conceptualization: Joseph A. Finlon, Greg M. McFarquhar
Formal analysis: Joseph A. Finlon, Greg M. McFarquhar, Thomas C. J. Hill, Paul J. DeMott
Funding acquisition: Greg M. McFarquhar
Investigation: Joseph A. Finlon, Wei Wu, Troy J. Zaremba, Greg M. McFarquhar
(continued)

Structure of an Atmospheric River Over Australia and the Southern Ocean: II. Microphysical Evolution

Joseph A. Finlon[1,2] , Robert M. Rauber[1] , Wei Wu[3] , Troy J. Zaremba[1] , Greg M. McFarquhar[3,4] , Stephen W. Nesbitt[1], Martin Schnaiter[5] , Emma Järvinen[5] , Fritz Waitz[5], Thomas C. J. Hill[6], and Paul J. DeMott[6]

[1]Department of Atmospheric Sciences, University of Illinois at Urbana-Champaign, Urbana, IL, USA, [2]Now at Department of Atmospheric Sciences, University of Washington, Seattle, WA, USA, [3]Cooperative Institute for Mesoscale and Microscale Studies, University of Oklahoma, Norman, OK, USA, [4]School of Meteorology, University of Oklahoma, Norman, OK, USA, [5]Karlsruhe Institute of Technology, Institute of Meteorology and Climate Research, Eggenstein-Leopoldshafen, Germany, [6]Department of Atmospheric Science, Colorado State University, Fort Collins, CO, USA

Abstract An atmospheric river affecting Australia and the Southern Ocean on 28–29 January 2018 during the Southern Ocean Clouds, Radiation, Aerosol Transport Experimental Study (SOCRATES) is analyzed using nadir-pointing W-band cloud radar measurements and in situ microphysical measurements from a Gulfstream-V aircraft. The AR had a two-band structure, with the westernmost band associated with a cold frontal boundary. The bands were primarily stratiform with distinct radar bright banding. The microphysical evolution of precipitation is described in the context of the tropical- and midlatitude-sourced moisture zones above and below the 0°C isotherm, respectively, identified in Part I. In the tropical-sourced moisture zone, ice particles at temperatures less than $-8°C$ had concentrations on the order of 10 L^{-1}, with habits characteristic of lower temperatures, while between $-8°C$ and $-4°C$, an order of magnitude increase in ice particle concentrations was observed, with columnar habits consistent with Hallett-Mossop secondary ice formation. Ice particles falling though the 0°C level into the midlatitude-sourced moisture region and melting provided "seed" droplets from which subsequent growth by collision-coalescence occurred. In this region, raindrops grew to sizes of 3 mm and precipitation rates averaged 16 mm hr^{-1}.

Plain Language Summary Atmospheric rivers (ARs) are long, narrow zones of enhanced horizontal poleward water vapor transport that have profound effects on the global hydrological cycle. This and a companion study are the first to analyze an AR affecting Australia and the Southern Ocean through an observational and modeling approach, respectively. There were two precipitation bands associated with the AR, which were primarily stratiform in character with an enhancement of radar reflectivity near the melting level. Part I showed that moisture in the upper part of the AR (above the 0°C level) was primarily sourced from the tropics, while moisture in the lower part (below the 0°C level) was primarily sourced from the middle latitudes. The microphysical evolution of precipitation through these two zones from cloud top to the ground within this AR is investigated. Ice particles forming and growing at altitudes above the 0°C level served as the "seeds" that allowed for further growth below the 0°C level as they melted and collided with droplets. The concentrations, shapes, and size distributions of the ice particles falling through each zone are presented and related to microphysical growth processes occurring within the bands.

1. Introduction

The pre-cold-frontal region within the warm sector of extratropical cyclones is sometimes associated with a narrow zone of enhanced horizontal poleward water vapor transport known as an atmospheric river (AR; Browning & Pardoe, 1973; Ralph et al., 2004; Zhu & Newell, 1998). Ralph et al. (2018) define an AR as a long, narrow, and transient corridor of strong horizontal water vapor transport that is typically associated with a low-level jet stream ahead of the cold front of an extratropical cyclone, the water vapor supplied by tropical and/or extratropical moisture sources. ARs can be thousands of kilometers long and hundreds of kilometers wide and play an important role in the global hydrologic cycle (Ralph et al., 2017).

Field experiments studying ARs have primarily targeted the Northeast Pacific. There the high frequency of landfalling extratropical cyclones combines with orographic enhancement to make ARs high-impact

Methodology: Joseph A. Finlon, Wei Wu, Troy J. Zaremba, Greg M. McFarquhar, Stephen W. Nesbitt, Martin Schnaiter, Emma Järvinen, Fritz Waitz, Thomas C. J. Hill, Paul J. DeMott

Project administration: Greg M. McFarquhar

Software: Joseph A. Finlon, Wei Wu, Troy J. Zaremba, Martin Schnaiter, Emma Järvinen, Fritz Waitz

Writing - original draft: Joseph A. Finlon

Writing – review & editing: Joseph A. Finlon, Wei Wu, Troy J. Zaremba, Greg M. McFarquhar, Stephen W. Nesbitt, Martin Schnaiter, Emma Järvinen, Fritz Waitz, Paul J. DeMott

precipitation events. Consequently, several studies have measured the properties of ARs in that region. The California Land-Falling Jets Experiment (CALJET), Pacific Land-Falling Jets Experiment (PACJET), and California Water Service (CalWater) field campaigns, for example, have obtained direct dropsonde measurements of the thermodynamic and kinematic structure of ARs (e.g., Neiman et al., 2016; Ralph et al., 2005, 2017). Satellite microwave imagers (Ralph et al., 2006; Wick et al., 2013) and radio occultation techniques (Ma et al., 2011; Neiman et al., 2008) have also been used to retrieve temperature and moisture properties through the vertical column of ARs. These studies have found that the greatest water vapor flux typically occurs in the lowest 3 km of the troposphere. Precipitable water values within ARs can be greater than 2 cm and integrated vapor transport often exceeds 250 kg m^{-1} s^{-1} (Dettinger et al., 2011; Neiman et al., 2008; Ralph et al., 2004, 2018; Rutz et al., 2014). Although the research focus has primarily been on ARs over the north Pacific, ARs have been shown to have considerable hydrological impact worldwide (Lavers & Villarini, 2013; Leung & Qian, 2009; Moore et al., 2012; Nakamura et al., 2013; Pfahl et al., 2014; Ralph et al., 2006; Waliser & Guan, 2017).

Microphysical processes acting within ARs have been interpreted primarily based on spaceborne and ground-based vertically pointing radar analyses and/or surface-based disdrometer measurements of drop size distributions (Cannon et al., 2017; Kingsmill et al., 2006, 2016; Martner et al., 2008; Matrosov, 2012, 2013; Matrosov et al., 2016; Neiman et al., 2017; White et al., 2015). These studies together show that precipitation from landfalling northeast Pacific ARs in mountainous regions can be characterized as a "seeder-feeder" process (Bergeron, 1965), where ice crystals forming in AR flow and growing by vapor deposition, riming, and aggregation fall through the melting layer into an orographically forced feeder cloud where precipitation continues growth through warm rain processes. White et al. (2003) found that 44% of the precipitation from 3 months of AR events in the Pacific Northwest could be attributed to the seeder-feeder process based on profiling radar observations. The seeder-feeder process does not always occur. Non-bright band signatures have been identified in some storms where precipitation growth is limited to condensation and subsequent droplet coalescence (Martner et al., 2008; Zagrodnik et al., 2018).

Although significant progress has been made in interpreting microphysical processes from remote sensing and surface-based measurements, studies that directly measure particle size distributions and habits through the depth of ARs and relate them to microphysical growth processes through the atmospheric column are rare. A target of opportunity to collect high spatiotemporal resolution in situ measurements of the structure and microphysics within an AR over Australia and the Southern Ocean occurred on 28–29 January 2018 during the Southern Ocean Clouds, Radiation, Aerosol Transport Experimental Study (SOCRATES). This paper investigates the microphysical evolution of particles within this AR using a vertically pointing Doppler radar and microphysical instruments aboard the National Science Foundation/National Center for Atmospheric Research (NSF/NCAR) Gulfstream-V (G-V) aircraft. The aircraft made two horizontal passes at −12°C and −20°C across the AR and descended through its vertical depth on its landing approach to Hobart International Airport in Tasmania. The microphysical observations from these transects are interpreted in the context of results of Rauber et al. (2020, hereafter Part I). In Part I, a water vapor tracer within the Weather Research and Forecasting model was used to show that as flow within the AR moved over the Southern Ocean, 50–60% of moisture above the 0°C level sourced from the tropics, while moisture below the altitude of the 0°C isotherm sourced primarily from the midlatitudes.

The remainder of the paper is organized as follows. Section 2 details the data sources, flight strategy, and the methodology employed to process the microphysics and radar data. The physical structure of the AR is discussed in section 3. The microphysical structure of the rainbands composing the AR is discussed in section 4. A discussion of the microphysical processes as they relate to moisture sources within the AR is presented in section 5, while key findings are given in section 6.

2. Data and Methodology

2.1. HIAPER Cloud Radar

The radar employed on the G-V was the High-Performance Instrumented Airborne Platform for Environmental Research (HIAPER; University Corporation for Atmospheric Research (UCAR)/NCAR, 2014) Cloud Radar (HCR), an airborne, W-band, Doppler research radar that fits within an underwing pod (Ellis et al., 2017). The HCR transmits at 94.4 GHz (3 mm wavelength) and was positioned at nadir

during all transects through the AR. The G-V was never above cloud top during the transects, so the cloud top altitude could not be determined from the radar data. Cloud top height and temperature at the location of the G-V were instead estimated from Himawari-8 geostationary satellite retrievals (see section 2.3). Equivalent radar reflectivity factor (Z_e, hereafter, reflectivity) and vertical Doppler radial velocity (V_r) measurements are reported in this paper. Calibrations were routinely performed during SOCRATES to develop correction factors for the Z_e and V_r measurements. A series of noise-source calibration procedures to develop correction factors for the Z_e measurements was performed by measuring changes in the receiver gain with a noise signal, which was insensitive to temperature changes (UCAR/NCAR, 2018a). Clear air ocean scan calibrations were also performed following the methodology of Li et al. (2005) to calculate the normalized radar cross section bias of the HCR (UCAR/NCAR, 2018b). Following Liebe (1985) and International Telecommunication Union (2013), attenuation by atmospheric gases was calculated and corrections applied to Z_e. Due to the high transmission frequency of the HCR (94.4 GHz), attenuation through liquid portions of the clouds was significant. No attempt was made to correct for attenuation by liquid-phase particles since the vertical distribution of liquid water content beneath the plane was unknown. The reflectivity data should thus not be interpreted quantitatively, as the radar signal penetrated through supercooled liquid water (SLW) layers above and rain below the radar bright band across the AR. The V_r was corrected for platform motion following Ellis et al. (2017) and Rauber et al. (2017). Radar gates were masked if the normalized coherent power was less than 0.16 to eliminate noise.

2.2. Microphysics Measurements
2.2.1. Liquid Water Content and Cloud Droplet Spectra
A Rosemont Icing Detector (RID) was used at $T < -5°C$ to identify when SLW was present based on the voltage change (converted from a frequency measurement) as ice accreted on a vibrating sensing element (Baumgardner & Rodi, 1989). A King probe (Bradley & King, 1979; King et al., 1978) provided measurements of water content (KWC). The King probe can be used without correction for measuring the liquid water content (LWC) of droplet distributions with median volume diameters less than about 40 μm, but as the medium volume diameter increases, there is a gradually diminishing response (Biter et al., 1987). Since past studies (e.g., Cober et al., 2001) have shown the King probe can respond by as much as 20% on average to ice water content, KWC measurements are not exclusively related to supercooled liquid water in mixed-phase and ice-phase clouds. A cloud droplet probe (CDP; Lance, 2012; Lance et al., 2010) provided a second measure of liquid water content through the integration of cloud droplet size distributions for $2 < D < 50$ μm.

2.2.2. Particle Image and Angular Light Scattering Observations
Cloud particle stereo-microscopic images were collected using the Particle Habit Imaging and Polar Scattering (PHIPS) probe (Abdelmonem et al., 2016; Schnaiter et al., 2018) and used to examine morphological properties of small cloud particles in the size range from $20 < D < 700$ μm for ice and $50 < D < 700$ μm for droplets. The PHIPS provides brightfield microscopic images at a maximum optical resolution of 2.5 μm using two camera-telescope assemblies and a pulsed illumination laser. The PHIPS instrument also has a single-particle polar nephelometer that consists of a continuous wave scattering laser and a ring of detectors at equiangular distances. The recorded single-particle angular light scattering function can be used to provide information on the phase of the particle. High-resolution images from the PHIPS are used herein to help interpret particle imagery from optical array probes (OAPs).

2.2.3. OAP Data
A 2D-Stereo (2D-S) probe was used to determine particle size distributions (PSDs), mass distribution functions, projected particle area, and other particle shape properties from shadowing on photodiode arrays from liquid- and ice-phase hydrometeors. The 2D-S has an optical resolution of 10 μm and imaged particle sizes spanning $0.01 < D < 3.2$ mm. Particles smaller than 0.05 mm are not considered here because ambiguities in the probe's depth of field and sample area for these particles make their concentrations highly uncertain (Baumgardner & Korolev, 1997; Jackson et al., 2012). Although a 2D-Cloud (2D-C) probe was also used during SOCRATES, particles were occasionally sized improperly or not at all when optical fogging resulting from condensation onto the mirrors occurred. The 2D-S was thus used for $D > 0.05$ mm.

The 2D-S data were processed using the University of Illinois/Oklahoma OAP Processing Software (McFarquhar et al., 2018; Wu & McFarquhar, 2019), which calculates morphological properties for individual particles (e.g., maximum dimension, projected area, area ratio, perimeter, and habit) and determines PSDs for each second of flight. The habit was determined using the Holroyd (1987) algorithm. Only

particles having their center within the OAP field of view were accepted so that the uncertainties in determining particle size from reconstruction were minimized (Field, 1999; Finlon et al., 2019; Heymsfield & Baumgardner, 1985). The 2D-S probe was fitted with antishattering tips, which should limit the impact of shattered artifacts (e.g., Korolev et al., 2011). Nevertheless, as in Korolev et al. (2011, 2013) and Jackson et al. (2014), a shattering removal algorithm was used to further reduce the impact of shattered artifacts on the PSDs. The shattering removal algorithm follows Field et al. (2006) by examining the distribution of interarrival times between particles entering the probe's sample volume (Field et al., 2003). The distribution is bimodal when shattered artifacts are present, with naturally occurring particles belonging to the mode with longer interarrival times and shattered artifacts belonging to the mode with shorter interarrival times. The minimum frequency between the peaks of the bimodal distribution was used as a threshold, which was constant throughout the flight, and particles whose interarrival time was below the determined threshold were rejected. For the periods analyzed in this study, approximately 10% of particles were rejected for having an interarrival time below the determined threshold.

2.2.4. INP Data

Ice nucleating particle (INP) measurements on this flight were not made directly within the AR but rather were made in cloud-free air throughout the flight over the Southern Ocean, both in the free atmosphere and the marine boundary layer (MBL). In Part I, it was shown that over 50% of the moisture above the 0°C isotherm originated in the tropics, while moisture in the lower atmosphere ascended within the bands from the MBL, so INP likely entered the AR from both altitudes.

INP data were collected in two ways. Aerosols were sampled outside of cloud regions from the HIAPER modular inlet (Stith et al., 2009) and processed with the Colorado State University Continuous Flow Diffusion Chamber (CFDC) and Ice Spectrometer (IS) instruments. Collection and processing methods followed are described in detail by Levin et al. (2019). The IS was used to measure the immersion freezing INP concentrations versus temperature for aliquots of total particle suspensions created with ultrapure water rinses from collected in-line filters. For this case, single precleaned filters were repeatedly sampled above and below the lowest cloud layers topping the MBL, integrating volumes (320–380 L) over a range of latitudes (54.2°S to 61.7°S) during aircraft profiling at different altitudes. The CFDC processed particles in real time in these same cloud-free regions. Essential details of CFDC processing included the requisite use of a 2.5 µm aerodynamic impactor for dried particles upstream of entry to the CFDC and operational relative humidity mostly in the nominal 105% range to stimulate immersion freezing for the closest correspondence to the IS data (De Mott et al., 2017). The lower temperature limit of the IS is typically −28°C. The CFDC temperature range is determined based on its sample volume (1.5 L min^{-1}) and the INP concentrations in each scenario. It was operated from −27°C to −32°C during SOCRATES, and 1 Hz data was reprocessed to the several minute intervals for each level leg above and below cloud in order to improve statistics. Corrections were applied for frost background in the CFDC on the basis of alternate sampling of prefiltered air, and through processing of field "blank" filters during SOCRATES for the IS, as described in the abovenoted publications. Uncertainties are given as 95% confidence intervals for both sets of data, as in past studies.

2.3. Satellite Retrievals

The cloud retrieval data set from the Himawari-8 satellite was available every 10 min at a nominal horizontal resolution of 2 km at nadir. A series of retrieval algorithms was developed by the NASA Satellite ClOud and Radiation Property retrievals System (SatCORPS) group to retrieve cloud top altitude (CTA) and temperature (CTT), among other cloud properties (Smith & Minnis, 2018; see also Minnis et al., 2008, 2011). The CTA and CTT Himawari-8 product was used to obtain CTT and CTA every 10 s along the G-V flight track by determining the value of the nearest neighbor pixel to the G-V within 5 min of the aircraft's position.

The dual-frequency precipitation radar (DPR) onboard the Global Precipitation Measurement (GPM) Core Observatory provided a vertical profile of the precipitation structure during the AR event. Reflectivity from the Ku-band (13.6 GHz) swath diagnosed two precipitation bands associated with the AR at the time of the overpass (section 3; see also Part I). The horizontal resolution is 5 km and vertical resolution 250 m at nadir, with a swath width of 245 km (Hou et al., 2014).

3. Physical Structure of the AR

The synoptic-scale structure of the AR was presented in Part I. Here the focus is the observed mesoscale and microscale structure as the G-V crossed and descended through the AR during departure and return near Hobart. The flight track at these times is superimposed on retrieved Himawari cloud top temperature and altitude in Figures 1a–1d. Figure 1e shows a Ku-band reflectivity profile of the AR from a GPM overpass approximately 13 hr after Figures 1c and 1d. HCR cross sections of Z_e and V_r along the G-V track across the AR appear for the departure and return legs in Figure 2. The gray regions above the flight tracks in Figure 2 are estimates of cloud depth above the aircraft based on Himawari-derived cloud top altitudes at the aircraft location.

The AR exhibited a double-banded structure during the G-V transit to (Figures 1a and 1b) and from (Figures 1c and 1d) the Southern Ocean and during the GPM overpass 13 hr later as evidenced by two distinct and continuous regions of enhanced Z_e reaching the surface (Figure 1e). Dropsondes launched across the AR (Part I) showed that the westernmost rainband (RB1) was directly along and over the cold front, while the easternmost rainband (RB2) was prefrontal. The bands ranged from 50 to 80 km wide. The G-V crossed RB1 and RB2 at −10°C on departure and at −20°C on return. The ascent and descent occurred within RB2. Detailed measurements after takeoff during the ascent through RB2 were incomplete because instruments were only brought online following takeoff during these passes. Microphysical analyses presented here are therefore limited to the departure leg through RB1, the return leg through RB2, and the descent through RB2 following an aircraft turn back into the band (Figures 1c and 1d).

At takeoff at 2255 UTC on 28 January 2018 the AR was located directly over Hobart. The aircraft ascended and reached a cruising altitude of 6.1 km (−10°C) by 2305 UTC, reaching RB1 at 2310 UTC. The aircraft flew through RB1 and the anvil region over the front, where the mean CTA was 8.3 ± 1.1 km and mean CTT was −25.4 ± 7.6°C (Figures 1a and 1b). The estimated CTA together with the radar data imply that the depth of the anvil region ranged from 3 to 3.5 km (Figures 2a and 2b). Radar cross sections also show a shallow cloud layer below the anvil region associated with surface-based postfrontal convection. The aircraft exited the AR anvil's western edge by 2340 UTC and then continued southward over the Southern Ocean (see Part I; Figure 2).

On return from the Southern Ocean, the G-V climbed to 8 km (−20°C) prior to reaching the AR and entered its western side at 0455 UTC on 29 January (Figures 1c and 1d). The aircraft crossed RB1 and RB2 at a constant altitude of 8 km and then turned northwest and began a descent at 0550 UTC through RB2 to the Hobart airport, landing at 0605 UTC (Figures 2c and 2d). The clouds composing the AR were deeper upon return, with a mean CTA of 11.1 ± 1.5 km in the anvil and RB1 and 10.7 ± 1.2 km in RB2. CTTs were also lower, with a mean CTT of −44.6 ± 10°C in RB1 and −41.1 ± 8.7°C in RB2 (Figure 1d). During both passes across the AR, the HCR radar reflectivity was attenuated, sometimes with complete elimination of the signal before reaching the ocean surface. Attenuation was associated with rain below the radar bright band and regions of SLW above the melting level. The impact of SLW on the microphysical evolution of particles falling within the AR is considered in the next section. To facilitate understanding of the microphysical evolution of particles falling through the AR rainbands, the data will be presented by considering each rainband comprising the AR separately.

4. Microphysical Structure of Rainbands Within the AR

4.1. Frontal Rainband RB1

The G-V made a constant-altitude pass through RB1 and the western anvil region at −12°C (6 km) on departure between 2313 and 2337 UTC 28 January and at −20°C (8 km) on return between 0507 and 0523 UTC 29 January. The higher altitude pass at the lowest temperature is considered first (Figures 3a and 3b). At 0508 UTC, the CTA was 12.5 km and the CTT was −53.9°C. Based on negligible KWC values and CDP particle concentrations and the absence of triggering of the RID probe, no supercooled water was present at the aircraft altitude (Figures 3d and 3e). Ice particle concentrations (N_{2DS}; $0.15 < D < 3.2$ mm) within RB1 at −20°C averaged 10.7 ± 5.9 L^{-1} across the anvil region (Figure 3e), where the uncertainty estimate is the standard deviation in the 1 s concentrations. The Holroyd (1987) habit classification of the 2D-S images identified irregular crystals as the dominant habit followed by bullet rosette crystals for particles larger than
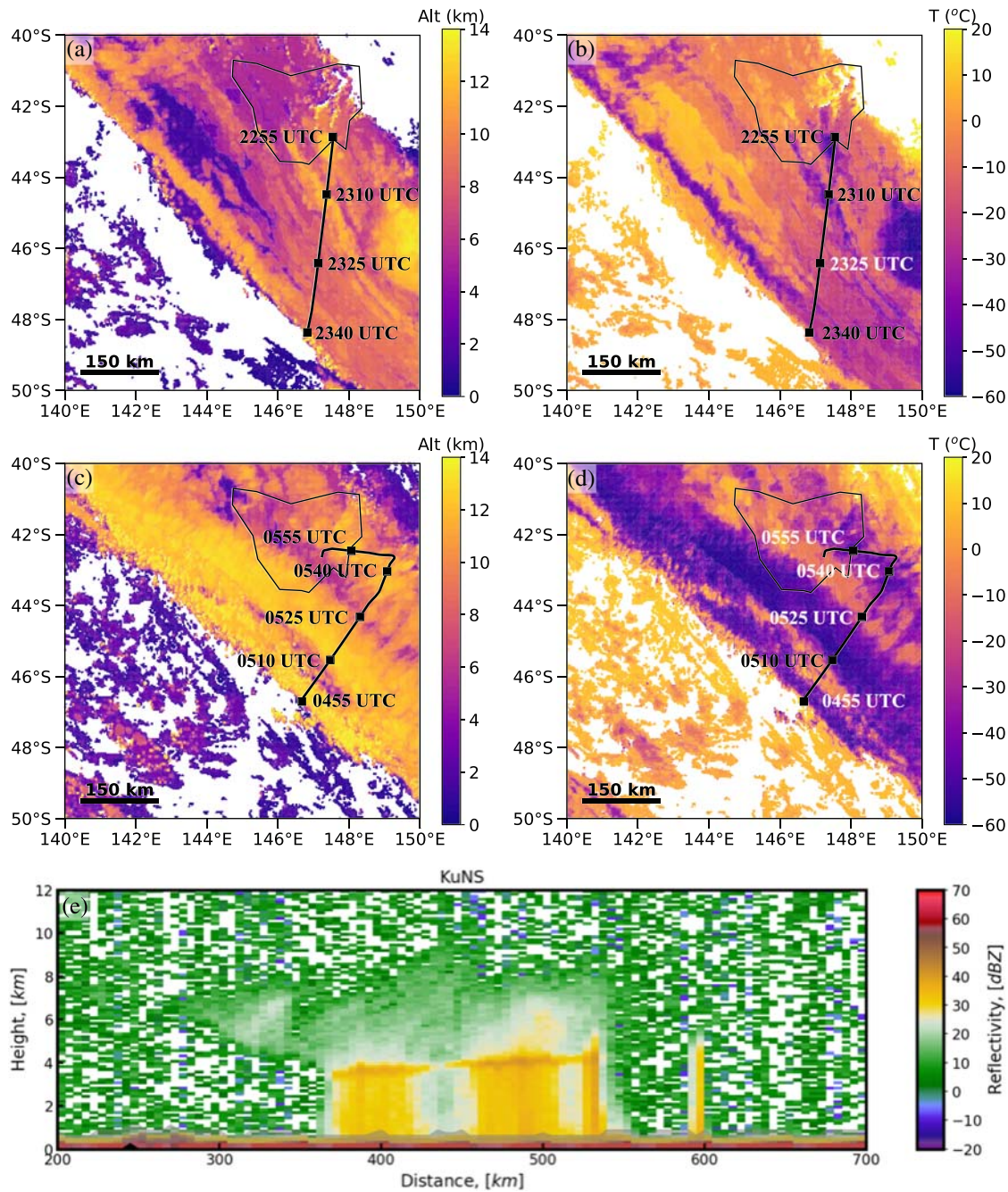
Figure 1. Retrieved cloud top height (a, c) and cloud top temperature (b, d) from the Himawari-8 satellite valid at 2320 UTC 28 January (top) and 0530 UTC 29 January 2018 (middle). The G-V flight track appears in black. A distance scale for (a)–(d) is given in (d). The aircraft position is annotated every 15 min. (e) Global Precipitation Measurement (GPM) profile of Ku-band equivalent radar reflectivity factor (Z_e) valid at 1908 UTC 29 January 2018 along GPM orbit 022280.

0.5 mm. It is likely that many of the 2D-S images classified as irregular were rosettes as well, given the −20°C temperature and that the observed particles were falling from colder cloud regions. Representative particle images from the PHIPS (Figure 3g) confirmed that bullet rosettes were common. Bailey and Hallett (2009) showed in field experiments that bullet rosettes falling through regions warmer than −40°C typically develop plate-like components since growth within the plate-like regime is favored between temperatures of −40°C and −20°C. Plate-like growth was common on bullet rosettes in PHIPS images at −20°C (Figure 3g). The $N(D)$ for $D \leq 0.7$ mm was characterized as a broad distribution of particle sizes
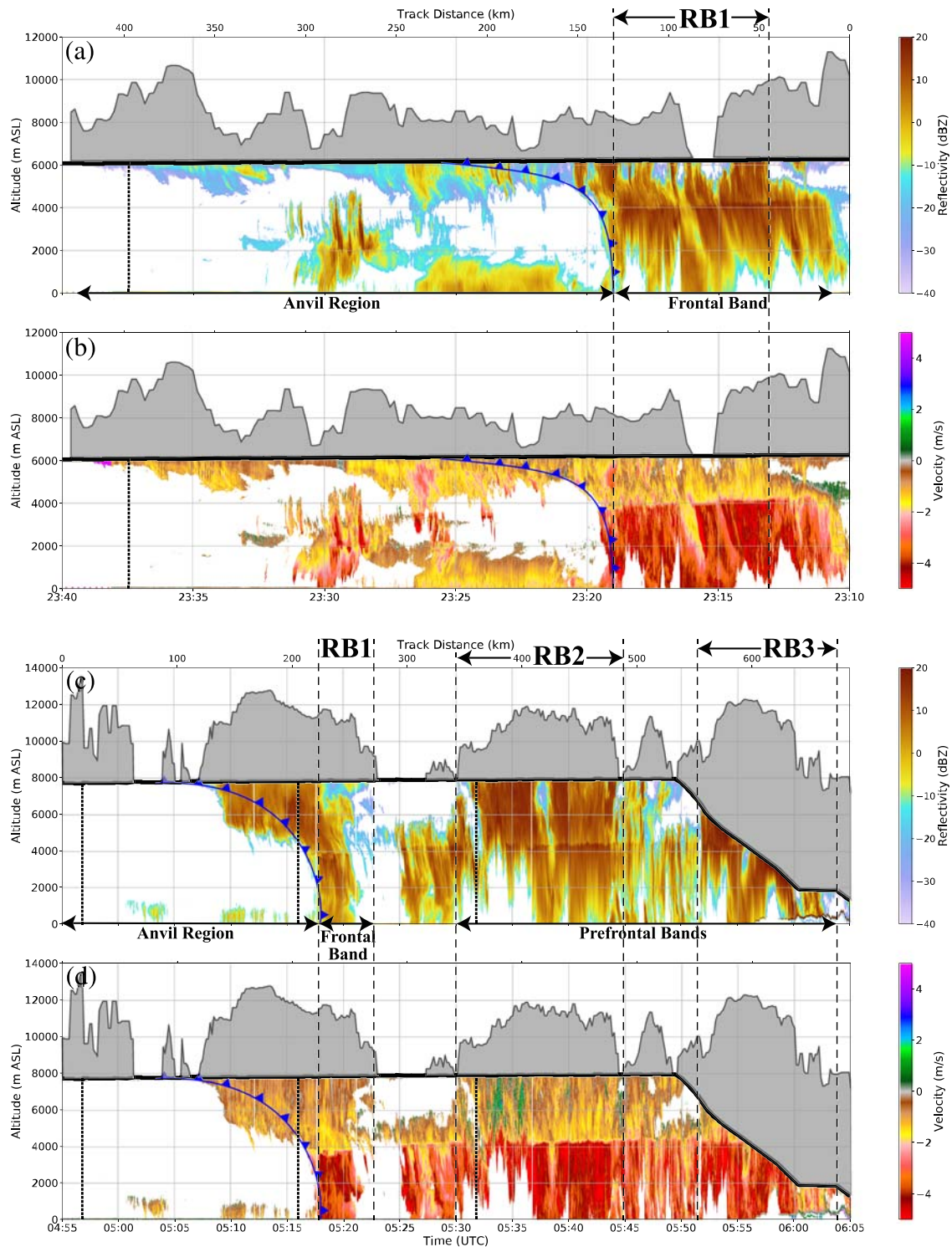
Figure 2. Radar cross section of (a, c) Z_e and (b, d) V_r from the HIAPER cloud radar (HCR) from (a, b) 2310–2340 UTC 28 January and (c, d) 0455–0605 UTC 29 January 2018. Aircraft location is denoted by the black line and the region shaded gray is bounded by the aircraft altitude and Himawari-8-estimated cloud-top height. The frontal band (RB1) and prefrontal band (RB2) and estimated frontal position based on dropsonde measurements (see Part I) are labeled. Dropsonde locations are shown by heavy dotted lines originating at the aircraft's altitude. Regions RB1 and RB2 indicate time segments used for expanded radar cross sections in Figures 3,5,7,9, and 12.
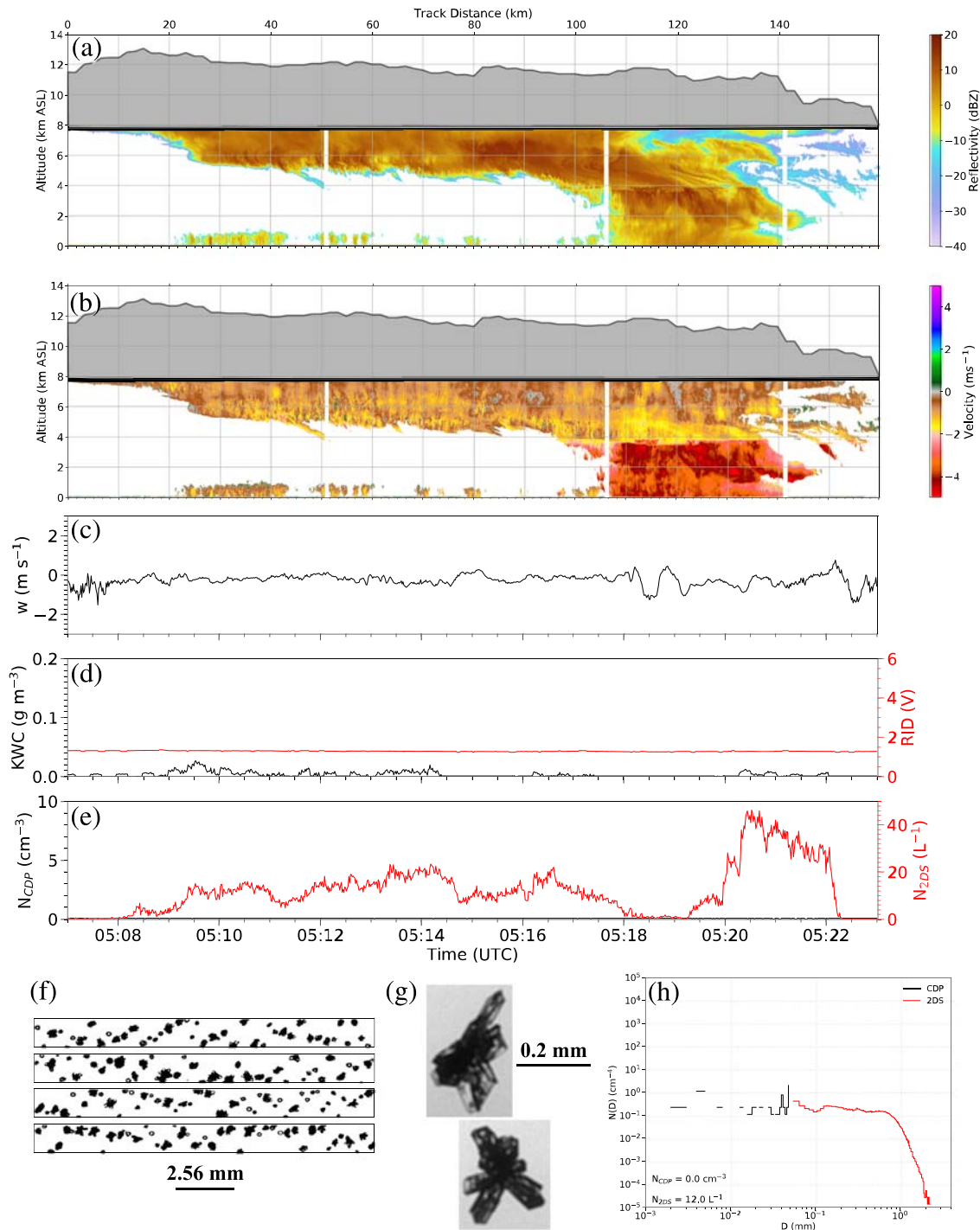
Figure 3. Radar cross sections of (a) Z_e and (b) V_r from the HCR for the anvil region and region labeled RB1 in Figures 2c and 2d (0507–0523 UTC 29 January 2018). Time series of (c) vertical velocity w, (d) KWC (black) and RID voltage (red), and (e) 10 s mean N_{CDP} (black) and N_{2DS} (red). Representative images from the (f) 2D-S and (g) PHIPS and (h) mean $N(D)$, N_{CDP}, and N_{2DS}. The flight-level temperature during the pass was −20°C.

(Figure 3h). Within RB1 on its east side, ice particle concentrations from the 2D-S increased to 17.3 ± 15.1 L^{-1} with a peak in $N(D)$ between 0.1 and 0.2 mm. Particles in this size range were identified as quasi-spherical ice from habit classification of the 2D-S images (Figure 3f), inspection of the PHIPS images (not shown), and examination of the angular scattering function (Schnaiter et al., 2018) resembling that of ice. The origin level of these spherical ice particles is unclear.
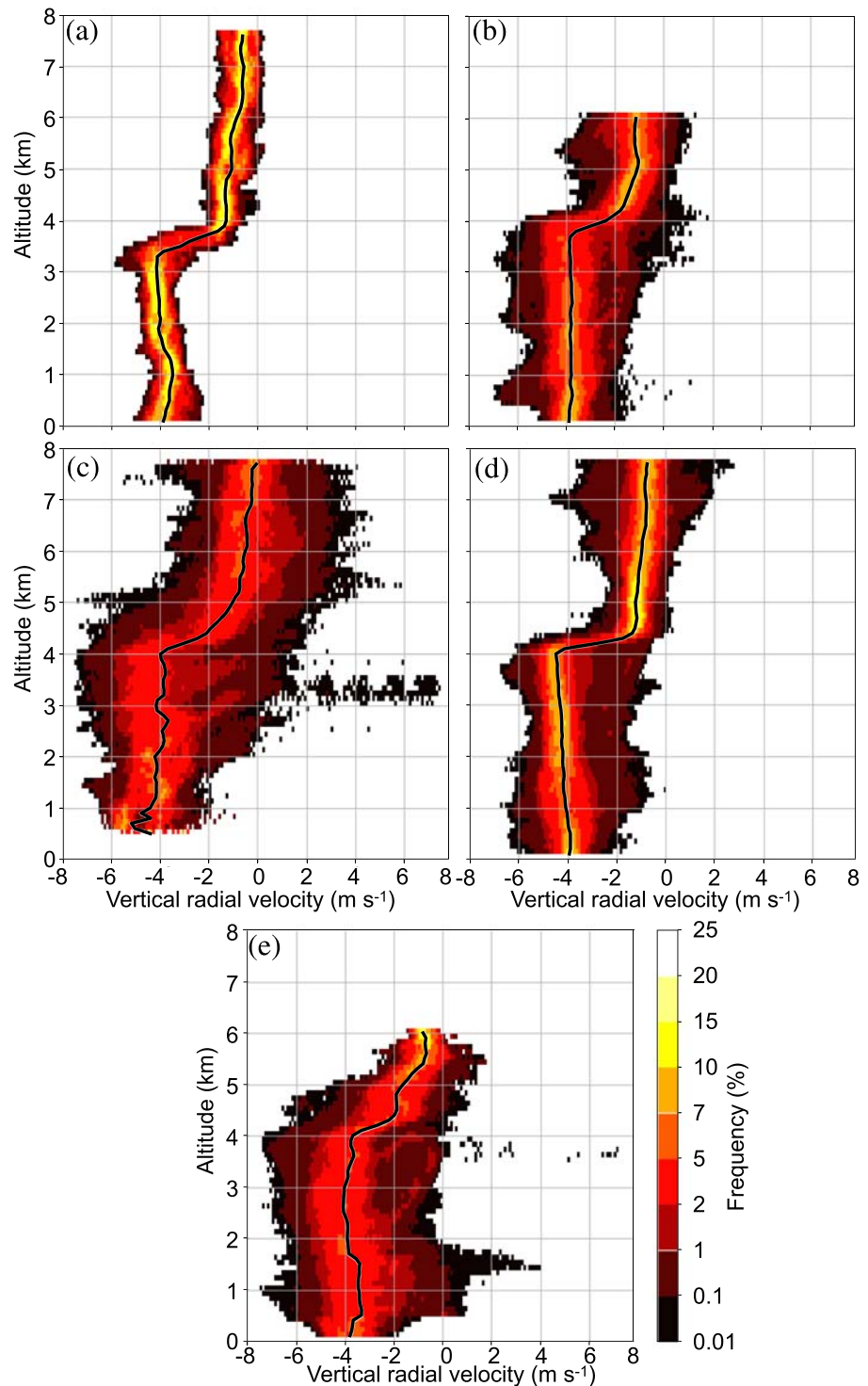
Figure 4. Contoured frequency by altitude diagrams (CFAD) of V_r from the HCR for (a) 0518–0520 UTC 29 January 2018, (b) 2313–2320 UTC 28 January 2018, (c) 0532–0536, (d) 0537–0544, and (e) 0552–0603 UTC 29 January 2018. (a, b) Corresponds to RB1 and (c–e) to RB2.

The HCR V_r measurements were analyzed using contoured frequency by altitude diagrams (CFADs; Yuter & Houze, 1995). On these diagrams, $\overline{V_r}$, the reflectivity-weighted median value of V_r, provides an estimate of the reflectivity-weighted terminal velocity of the particle ensemble (see review by Protat & Williams, 2011).
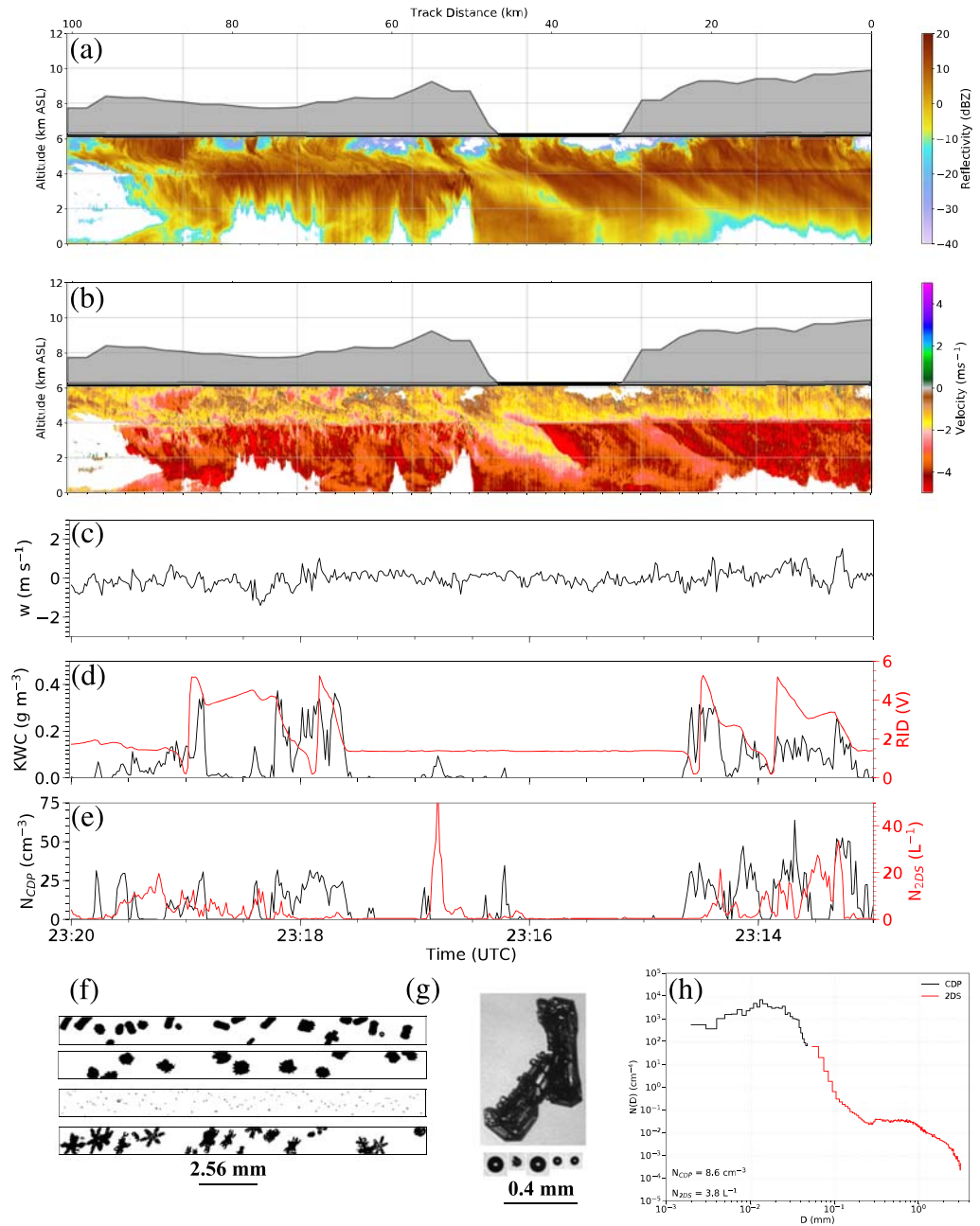
Figure 5. Same as in Figure 3 but for 2313–2320 UTC 28 January 2018 (region RB1 in Figures 2a and 2b). The flight-level temperature during the pass was −12°C.

The V_r measurements were binned by velocity in 0.1 m s^{-1} increments and by altitude in 100 m increments. Radial velocity measurements in the lowest 100 m were not considered to avoid contamination by the ocean surface or terrain.

The V_r CFAD for RB1 (0518–0520 UTC 29 January, Figure 4a) for the pass at −20°C shows a narrow distribution of V_r values, ranging between −2 and 0 m s^{-1}, between the aircraft altitude and the melting level (~3.8 km). $\overline{V_r}$ decreased with depth from −0.8 to −1.2 m s^{-1}, typical terminal fall speeds for single ice crystals (see summaries in Locatelli & Hobbs, 1974; Rosenow et al., 2014). The narrow spread of V_r implies that the precipitation band consisted of stratiform clouds. Below the bright band, V_r ranged between −5 and −2.5 m s^{-1} with $\overline{V_r}$ near −4 m s^{-1}. A slight broadening of the drop size distribution (DSD) in the lowest
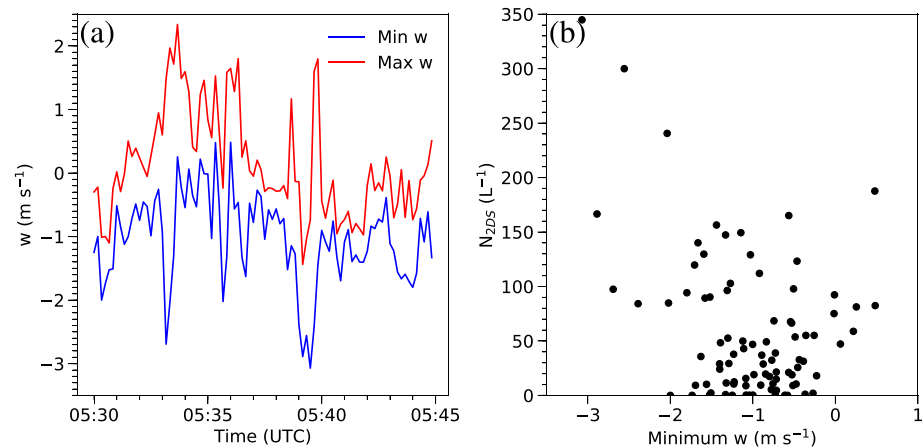
Figure 6. (a) Time series of the minimum (blue) and maximum w (red) for each 10 s interval and (b) N_{2DS} as a function of the minimum w for the same 10 s intervals between 0530 and 0545 UTC 29 January 2018.

km of the rainband is evident from the spread of V_r. There was no evidence for convective vertical motions in RB1 at the time of this pass.

The G-V also flew through RB1 at −10°C at an earlier time between 2313 and 2320 UTC. A series of precipitation fall streaks was evident at this time in the radar reflectivity field (Figure 5a). As the aircraft penetrated the fall streaks, CDP droplet number concentrations ranged between 25 and 50 cm^{-3}, KWC values exceeded 0.3 g m^{-3}, and the RID was triggered confirming the presence of SLW. The 2D-S $N(D)$ indicated a fairly broad distribution of ice particle sizes (Figure 5h), with the mode of higher concentrations between 0.4 and 1 mm primarily associated with rimed columnar ice crystals and irregular crystals, based on the habit classification of the 2D-S and PHIPS images (Figures 5f and 5g). The presence of mixed phase conditions at −10°C is consistent with an active riming process at this temperature.

As the aircraft penetrated the fall streaks, sharp transitions between regions of ice particles and regions dominated by smaller SLW droplets occurred. For example, droplet concentrations from the CDP increased to 33 cm^{-3} while ice number concentrations remained below 3 L^{-1} for the fall streak beginning at 231730 UTC (Figure 5e). The supercooled droplets, appearing as spherical PHIPS particles with a smooth perimeter, a Poisson (or Fresnel diffraction) spot in the center, and an angular scattering function consistent with that of liquid drops, ranged from 50 to 100 μm in diameter (Figure 5g). A response from the RID voltage was observed and KWC values approached 0.4 g m^{-3} within some of the fall streaks (Figure 5d). Measurements of vertical velocity (w) by the aircraft through the fall streak beginning at 231730 UTC indicated a weak ~1 m s^{-1} updraft (Figure 5c), which was sufficient to transport smaller cloud droplets from lower altitudes up to the aircraft's position.

The aircraft flew into and out of another series of fall streaks between 231830 and 231930 UTC, where w ranged between −1.5 and 0.7 m s^{-1} (Figure 5c). The fall streaks during this 1 min period again contained a mixture of ice particles and supercooled droplets, with KWC increasing to maxima ranging between 0.15 and 0.4 g m^{-3} (Figure 5d). As the G-V flew between fall streaks during this period, dendritic particle images appeared on 2D-S images (bottom strip, Figure 5f). Laboratory studies by Bailey and Hallett (2009) imply that these particles formed between −18°C and −12°C and, therefore, must have fallen to the altitude of the aircraft through the mixed phase region, as evident by rimed structures apparent on PHIPS images (Figure 5g). Aggregation also was likely at −10°C, as ice particles as large as 3 mm were observed in $N(D)$ (Figure 5h).

Between the aircraft level and the melting level, $\overline{V_r}$ decreased from −1 to −2 m s^{-1}, with higher fall speeds consistent with ice particle growth by riming as particles fell between −10°C and 0°C. Below the melting level, $\overline{V_r}$ was −4 m s^{-1}, characteristic of submillimeter raindrops. The most extreme values of V_r approached 1 m s^{-1} at temperatures less than 0°C and −1 m s^{-1} at temperatures greater than 0°C. The narrow spread in V_r was consistent with stratiform rather that convective vertical motions within RB1. The presence of clouds,
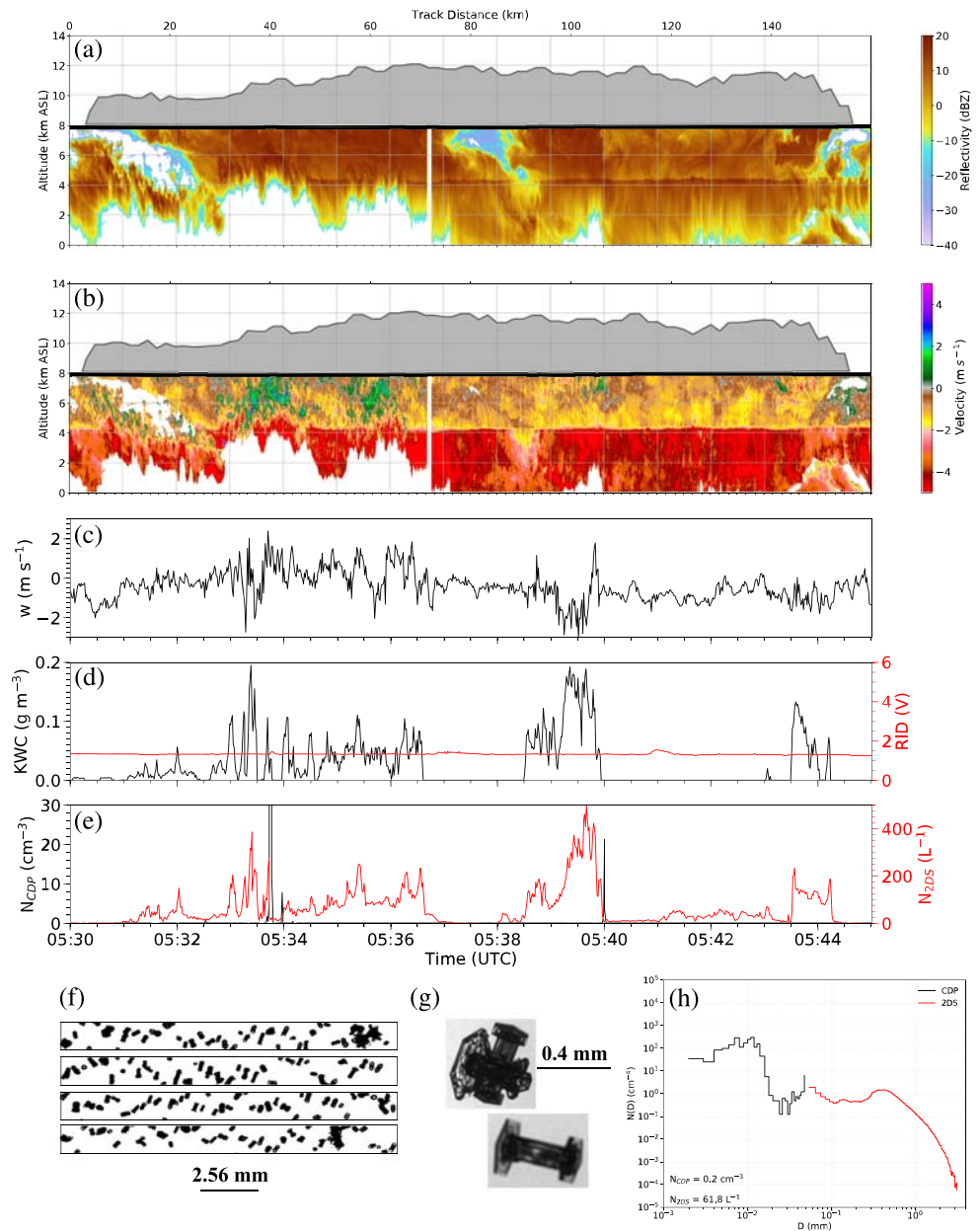
Figure 7. Same as in Figure 3 but for 0530–0545 UTC 29 January 2018 (region RB2 in Figures 2c and 2d). The temperature during the pass was −20°C.

nonconvective vertical motions along the cold front, and riming below −10°C are consistent with the interpretation in Part I that vertical air motions within RB1 were forced by the ageostrophic circulation along the front rather than convection and that ice particles from aloft within the tropical airstream seeded the lower level cloud region below the melting level.

4.2. Prefrontal Rainband RB2

The flight segment across RB2 at −20°C (0530–0545 UTC; Figure 7) was characterized by stronger updrafts and downdrafts compared to RB1 at −20°C based on CFADs of V_r (Figures 4c and 4d) and measurements of w at the aircraft's altitude (Figure 6a). Subtracting $\overline{V_r}$ to estimate updraft speed, the strongest updrafts between 5 and 8 km ASL approached 5 m s^{-1} and the strongest downdrafts approached −3 m s^{-1} between 0532 and 0536 UTC (Figure 4c). The updraft region was associated with complete attenuation of the HCR signal at lower altitudes (Figures 7a and 7b), consistent with the presence of SLW below the aircraft
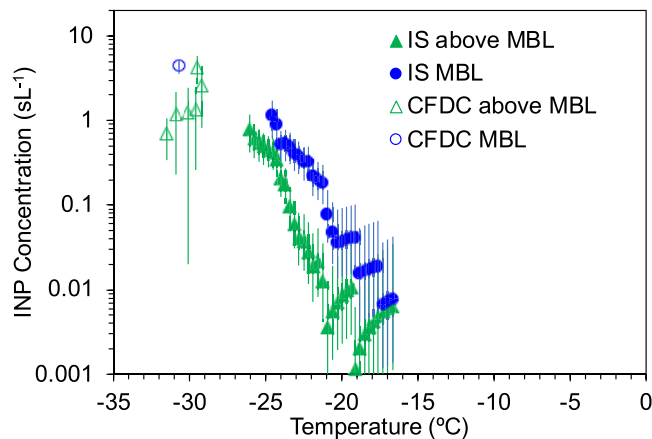
Figure 8. Ice nucleating particle measurements via CFDC and IS methods (see text) for cloud-free air over the Southern Ocean region during the research flight on 29 January 2018. The CFDC data represent several minute legs at approximately 160 (in MBL), 1,600 and 7,700 m MSL (above cloud), while IS data represents longer integrated collections over a latitude range within the MBL at 160 m and above lowest clouds at ~1,600 m MSL.

altitude in the updrafts. The updrafts did not persist into the eastern part of RB2 between 0537 and 0544 UTC (Figure 4d).

At the G-V altitude, the standard deviation of w was 2.7 times greater across RB2 than within RB1 at −20°C. The minimum and maximum w for each 10 s period at −20°C in RB2, shown in Figure 6a, indicates that downdrafts were occasionally on the order of 2–3 m s^{-1}. Those downdrafts coincided with reductions in temperature of 4°C between 0535 and 0539 UTC as cooler, negatively buoyant air from above the G-V location descended across the flight path. Updrafts were occasionally on the order of 1.5–2.5 m s^{-1} at the G-V altitude. The G-V sampled downdrafts as large as 3 m s^{-1} and updrafts as large as 2 m s^{-1} during a 1 min period at the flight level (Figure 7c). Despite the stronger updrafts, SLW was absent across the pass at −20°C, except in local areas, based on CDP concentrations and the absence of triggering by the RID. Droplet concentrations from the CDP remained below 0.1 cm^{-3} during the period except for very localized regions where N_{CDP} approached 30 cm^{-3} (Figure 7e). The positive KWC measurements in Figure 7d coincided with trends in the 2D-S ice particle concentrations indicating that the King probe was responding to ice rather than SLW.

Number concentrations of ice were highly variable between 0530 and 0545 UTC, with N_{2DS} averaging 65 L^{-1} across the pass, with peak values exceeding 400 L^{-1}, with the N_{2DS} distribution skewed toward larger values (Figure 7e). Concentrations exceeded 100 L^{-1} for 17 10 s periods, with the highest concentrations corresponding to downdrafts of 2–3 m s^{-1} (Figure 6b). Representative 2D-S and PHIPS images shown in Figures 7f and 7g for RB2 illustrate primarily columnar crystals in the 0.3–0.6 mm size range, some capped by plates. The occurrences of columns corresponded to peaks in $N(D)$ between 0.3 and 0.6 mm, in regions where concentrations locally exceeded 300 L^{-1}. Bailey and Hallett (2009) found that columns originating from lower temperatures and falling into the plate-like growth regime where ice supersaturations are between 0.1 and 0.2 can be hollow or be capped by plates, consistent with the particles observed in Figure 7.

The relation between downdraft speed, particle ice concentration, and particle habit (Figure 7) suggests that ice crystals from above the aircraft's location were transported in the downdrafts to the −20°C level where the measurements were made. These crystals thus formed within the tropical moisture airstream that was discussed in Part I. The low-level updrafts on the southwest side of the band (0532–0536 UTC 29 January in Figure 7) provide evidence that weak embedded convection was present in the lower part of RB2. Based on the inferred strong attenuation of the HCR signal, the updrafts in this region produced SLW below the flight level at −20°C, supporting riming of ice particles descending from above as they approached the melting level. Measured INP concentrations during the flight ranged from 0.5 to 1.0 L^{-1} at −25°C and 0.01 to 0.04 L^{-1} at −20°C (Figure 8), which was much lower than the 100–400 L^{-1} ice particle number concentrations observed. Although the relationship between downdraft speed and ice number concentrations suggests that higher concentrations of ice may have arrived at the aircraft level from colder temperatures, the orders of magnitude discrepancy between INP and ice particles concentrations at the aircraft level suggest that some secondary ice production process might have been active. The nature of that process, if it exists, could not be determined from the available data.

4.3. Descent Through Prefrontal Rainband RB2

The aircraft turned northwest and back into RB2 and began its descent from −20°C entering the easternmost part of the band at $T = -13$°C at 055140 UTC. Figure 9 shows the portion of the descent above the melting level. Particle size distributions for each 1°C temperature interval and corresponding 2D-S and PHIPS images appear in Figures 10 and 11, respectively. Between −13°C and −10°C, ice particles consisted of irregular aggregate assemblages at concentrations ranging from 5 to 10 L^{-1}. Little change occurred in the PSDs between these temperatures as ice particles fell from aloft. No supercooled water was present along the flight path, and weak downdrafts of 0 to −1.5 m s^{-1} were observed at the flight level. However, beginning at the
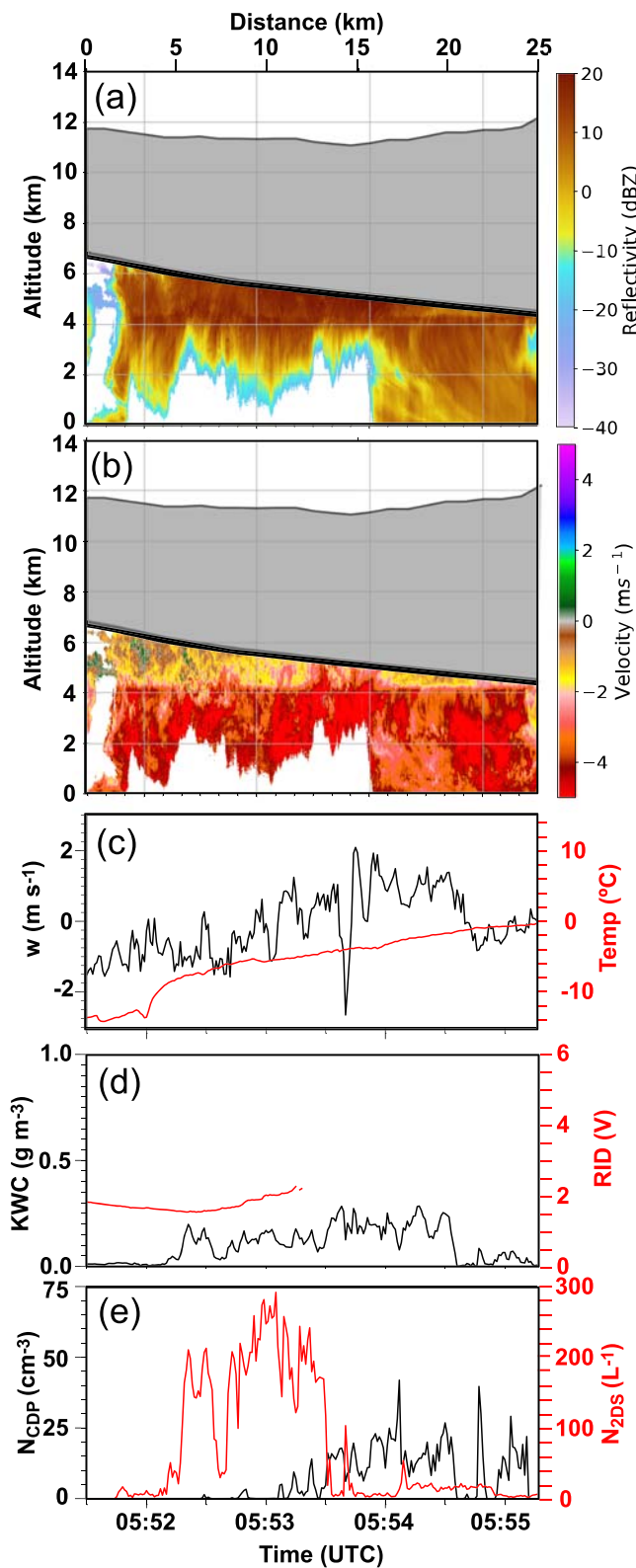
Figure 9. Same as in Figure 3 but for 055130–055530 UTC 29 January 2018. Time series of temperature also shown in (c) in red. RID measurements in (d) are not shown for $T > -5°C$.

−8.5°C level and continuing downward through the −4°C level, 2D-S ice particle concentrations increased by an order of magnitude to values of 100–200 L^{-1}. The $N(D)$ across this temperature range showed increases at all sizes, particularly in the size range 50–500 μm. Supercooled water first appeared near −6°C and was present from −6°C to the melting level, with droplet concentrations ranging between 5 and 40 cm^{-3}. The dominant particle habits between −8°C and −4°C transitioned to columnal crystals, columnal aggregates, and needles. Irregular particles were also present.

Since columnar habits were not observed at higher altitudes, these particles were most likely produced within the −8°C to −4°C temperature range. Hallett and Mossop (1974) and Mossop and Hallett (1974) showed that copious numbers of ice splinters could be produced during riming of large ice particles provided that the temperature ranged between −8°C and −3°C, and small liquid droplets ($D < 12$ μm) and large liquid droplets ($D > 25$ μm) were present. Choularton et al. (1978, 1980) and Griggs and Choularton (1983) later showed that the small droplets, upon riming, provide point sites for the larger droplets to attach and freeze, with the mode of freezing and probability of splinter production determined by temperature. Although the conditions required for the Hallett-Mossop mechanism were not present at the aircraft location between −8°C and −6°C at the time of sampling due to the absence of supercooled water, they were present at warmer temperatures. Given the order of magnitude increase in particle concentrations and the appearance of columnar habits, the observations are consistent with the Hallett-Mossop mechanism being active in RB2.

As the aircraft continued its descent and temperatures increased to values outside of the zone favorable for rime splintering, concentrations of ice particles with $D > 150$ μm decreased to 5–20 L^{-1}, a result consistent with the action of aggregation (Figure 11) and evidenced by an increase in the $N(D)$ for aggregates identified from 2D-S data. By 055440 UTC, temperatures at the aircraft level approached −1°C when the aircraft was within 300 m of the melting level. The mean $N(D)$ for the period shows particles as large as 3 mm (Figure 10); larger particles may have been present but were not included in the particle spectra because they exceeded the field of view of the 2D-S.

Measurements of $\overline{V_r}$ above the melting level (4.2 km; Figures 2d and 4e) decreased from −1 m s^{-1} at 6 km to −2 m s^{-1} near the melting level. The occurrence of $V_r \leq -2$ m s^{-1} close to the melting layer (Figure 4e) appears as a disruption in the radial velocity signal with more negative values along the radar bright band between 0553 and 0554 UTC (Figure 9b). Regions where V_r values ≤ -2 m s^{-1} extending above the melting level are related to the presence of SLW (based on the rapid attenuation of the radar signal) and riming of ice particles. Microphysical observations through a 10 s period when the G-V penetrated through a 1 km region where $V_r \leq -2$ m s^{-1} show an abrupt change in the types of particles observed between 055330 and 055340 UTC. An increase in the KWC from 0.1 to 0.3 g m^{-3} during the beginning of the 10 s period (Figure 9d) and N_{CDP} exceeding 10 cm^{-3} was accompanied by w values of 1 m s^{-1} (Figure 9b), implying that supercooled droplets were lofted from lower altitudes upward through the 0°C level. Riming and the associated increase in fall velocity as ice particles fell through the cloud of
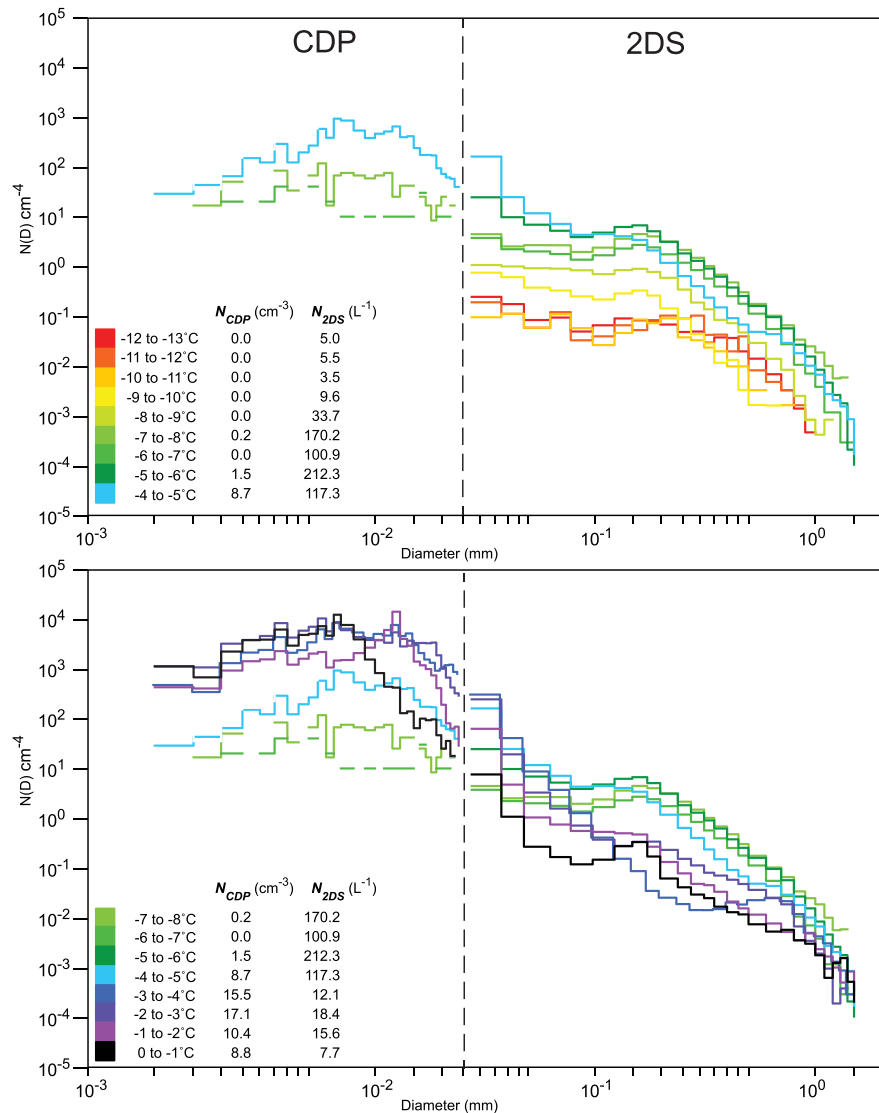
Figure 10. Particle size distributions every 1°C level for the descent through RB2 from −13°C to the melting level. Average CDP and 2D-S total particle concentrations within each temperature interval are given in the tables.

supercooled drops provides a possible explanation for the more negative V_r values observed at altitudes just above the melting layer.

The aircraft descended below the melting level by 055530 UTC and by 055540 UTC all ice was melted at temperatures greater than 1°C (Figures 12c and 13a). Below the melting level, $\overline{V_r}$ ranged between −4 and −3.5 m s^{-1}. Variability in the vertical velocities at the G-V altitude below the melting level (Figure 12c) result from variations in the distribution of raindrop sizes within the rainband as well as variations in vertical air velocity (Figure 4e). Based on model results from Part I, the larger drops at this altitude (4.3 km) developed as ice particles, from primarily tropical-sourced moisture above the 0°C level, melted (see Figure 12c, Part I). The model results of Part I also show that the majority of the water vapor at altitudes below the 0°C isotherm sourced from the midlatitudes below 4 km, ascending within the frontal zone with the ageostrophic circulation (see Figures 13b and 14 in Part I). This midlatitude-sourced moisture allowed for the production of many small droplets, with concentrations averaging 51.7 ± 38.1 cm^{-3} between 0°C and 10°C and values up to 153 cm^{-3} that were collected by lower concentrations of larger drops ($1.1 \leq N_{2DS} \leq 9.9$ L^{-1}) falling from aloft. Near 5°C, drops approaching 3 mm were observed (Figure 13b). The DSD during this time was characterized by a broad distribution of particle sizes and average precipitation rate P_r, estimated from the 2D-S
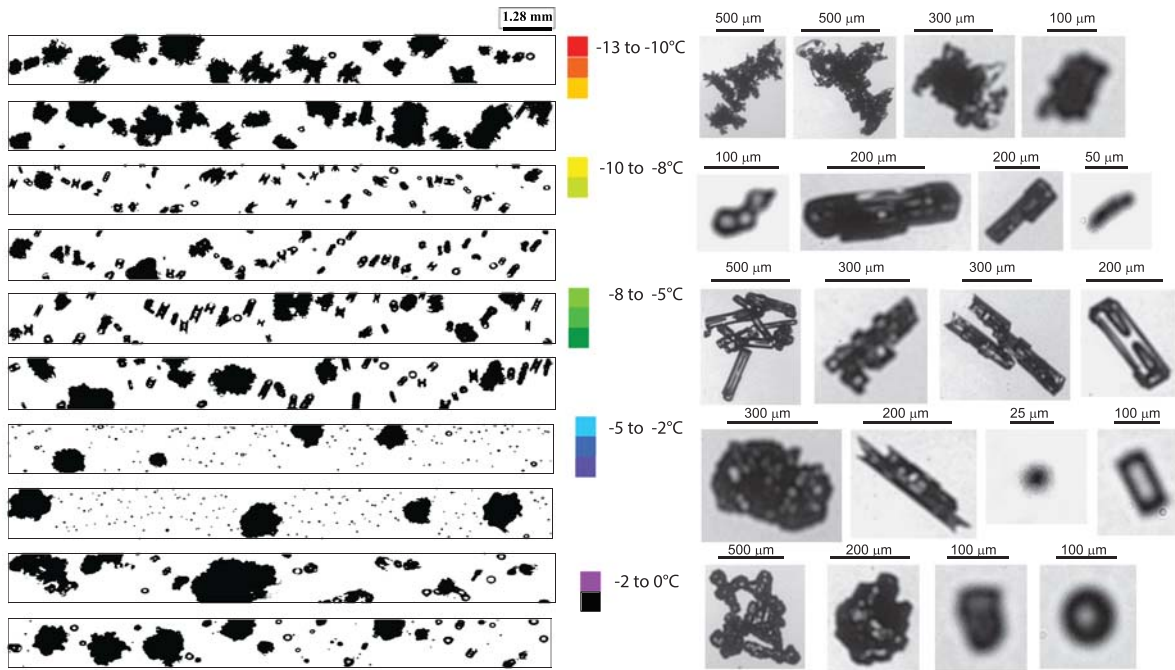
Figure 11. Representative images from the 2D-S and PHIPS for the descent through RB2 from −13°C to the melting level.

DSD, to be 16 mm hr^{-1} (Figure 12d). Values of P_r increased to 30 mm hr^{-1} (with locally higher amounts) by 0558 UTC 29 January as the G-V descended between the 0°C isotherm and the surface. The precipitation rate varied over a wider range locally as w fluctuated between −2 and 3 m s^{-1} at the aircraft altitude (Figures 12c and 12d). The presence of larger drops at lower altitudes shows that raindrops continued growth by coalescence as they fell to greater temperatures (Figure 13b). Maximum drop sizes of 3 mm were present until 0600 UTC when the G-V exited the main precipitation band.

5. Discussion

A conceptual model of the microphysical processes occurring within the AR that is consistent with the radar and microphysical observations appears in Figure 14. The AR consisted of a frontal band and a prefrontal band with cloud top heights extending above 12 km and cloud top temperatures as low as −50°C. Based on results from Part I and the observations herein, strong vertical velocities characteristic of deep convection were absent, although locally embedded convection occurred in the prefrontal band at middle altitudes between 5 and 8 km. The bands otherwise exhibited stratiform characteristics, with distinct radar bright bands present. Within the bands, the region between cloud top and the melting layer (4 km) consisted of particles that were sourced primarily from tropical moisture originating from northwest Australia. The layer between the melting level and surface consisted primarily of midlatitude-sourced moisture that was incorporated into precipitation through collision-coalescence with drops formed by ice particles falling through the melting level.

Within the tropical-sourced region, ice crystals originating near cloud top at temperatures below −40°C consisted of columns, bullet rosettes, and irregular particles. At −20°C, these rosettes exhibited plate-like features consistent with previous laboratory studies (e.g., Bailey & Hallett, 2009). Vapor deposition was the primary growth process at −20°C, where SLW was negligible. A greater presence of SLW at the −10°C flight level was consistent with the rimed appearance of ice crystals. The rimed particles included irregular assemblages, capped columns, and occasional dendrites, as particles continued to fall within regions where the vertical velocities were small ($w < 1$ m s^{-1}). Regions of localized stronger updrafts (1–5 m s^{-1}) were occasionally observed at the aircraft level in RB2, and greater concentrations of supercooled droplets either formed or were transported upward from lower altitudes in these regions.
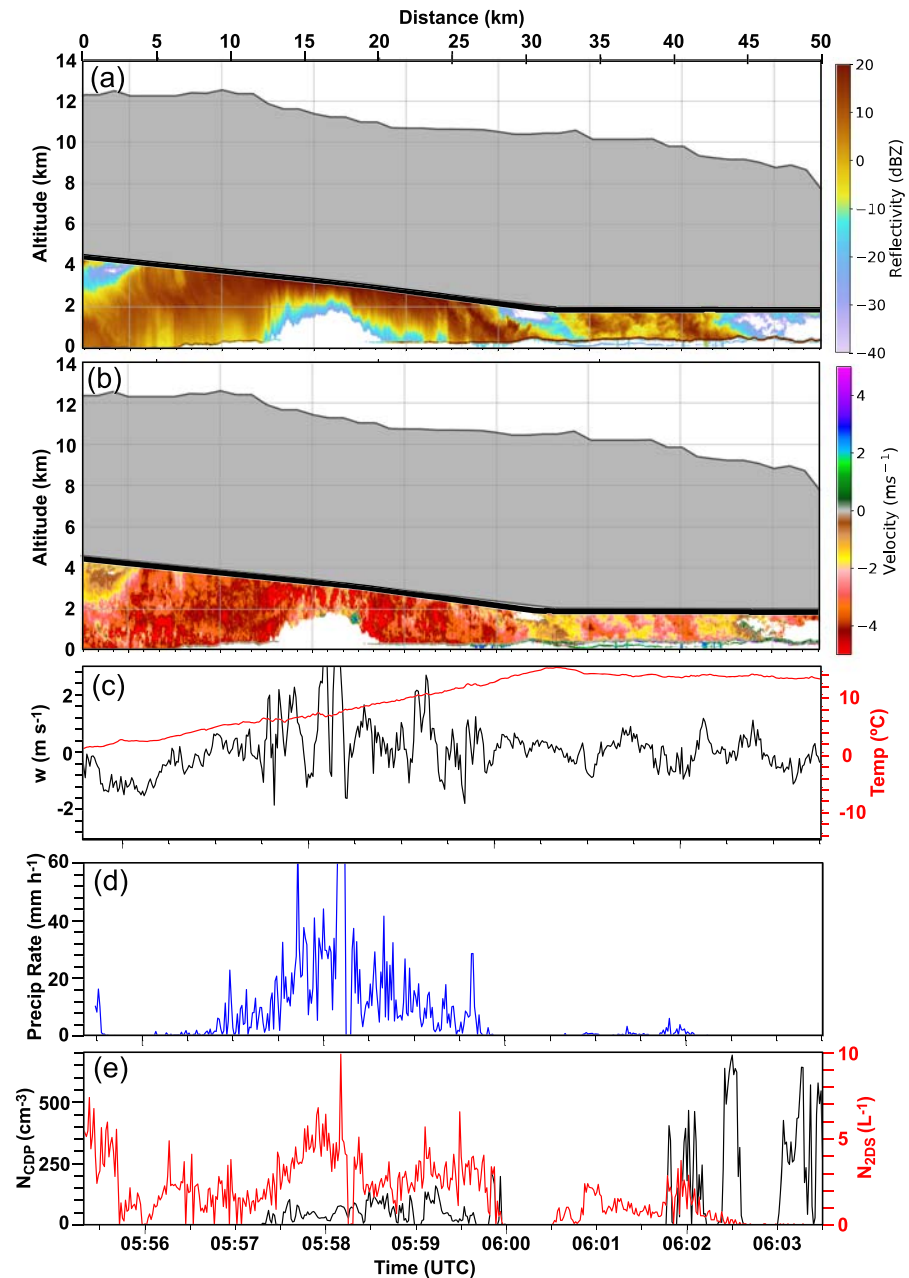
Figure 12. (a–c and e) Same as in Figure 9 but for 055430–060330 UTC 29 January 2018 (region RB2 between the surface and the 0°C level in Figures 2c and 2d). (d) Precipitation rate P_r derived from 2D-S DSDs.

Observations through the depth of the prefrontal band from −14°C to 0°C as the G-V returned from the Southern Ocean highlight changes in key microphysical processes. Ice multiplication presumably associated with the Hallett-Mossop process within the temperature zone from −8°C to −3°C was consistent with an order of magnitude increase in particle concentrations and the appearance of columnar crystals, columnar aggregates, and needle habits. Aggregation just above the melting layer reduced particle concentrations but allowed ice particles to grow as large as 3 mm before melting as they fell into the midlatitude-sourced moisture region below the 0°C isotherm. Within this region, low-level moisture promoted the production of small droplets with mean concentrations of 47 ± 30 cm^{-3} that were collected by lower concentrations of falling larger drops. Drop growth to diameters larger than 3 mm through collision and coalescence continued as the hydrometeors precipitated toward the surface.
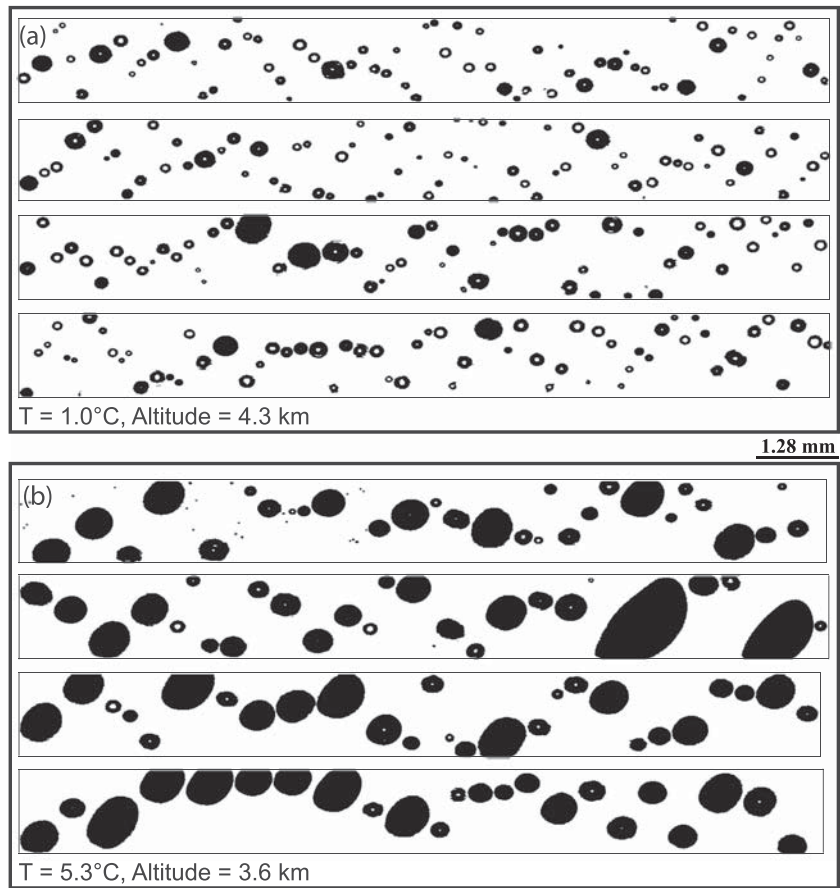
Figure 13. Typical particle images at 4.4 km, just below the melting level at 1.0°C, and at 3.6 km at 5.3°C, showing the growth of raindrops with depth in RB2.

As noted in the introduction, microphysical studies derived from ground-based vertically pointing radar analyses and/or surface-based disdrometer measurements of drop size distributions conducted in the Sierra Nevada during the landfall of northeast Pacific ARs show that precipitation can be characterized as
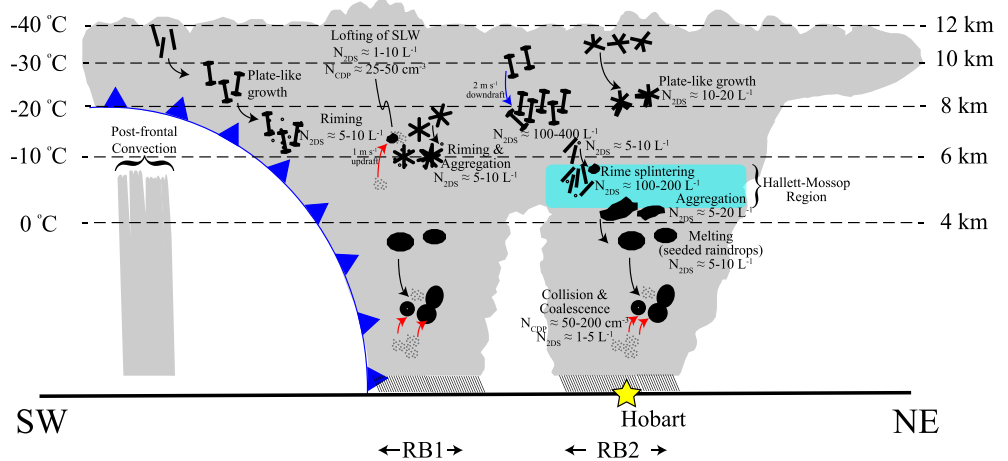

Figure 14. Schematic depicting the precipitation structure and processes observed within the AR. Number concentrations broadly represent values observed at the temperature indicated. Arrows denote the general transport of particles within the clouds.

a "seeder-feeder" process, where ice crystals forming in AR flow and growing by vapor deposition, riming, and aggregation fall through the melting layer into an orographically forced feeder cloud where precipitation continues growth through warm rain processes (Cannon et al., 2017; Kingsmill et al., 2006, 2016; Martner et al., 2008; Matrosov, 2012, 2013; Matrosov et al., 2016; Neiman et al., 2017; White et al., 2015). The microphysical evolution in this AR may be likened to a seeder-feeder process in that ice particles developed in moisture sourced from the topics in the upper part of the AR "seeded" the lower part of the AR, which consisted primarily of moisture from the midlatitudes, the boundary between the seeder and feeder zones being the 0°C isotherm.

6. Conclusions

This is the second paper describing an AR over Australia and the Southern Ocean observed during a target-of-opportunity flight during the SOCRATES. In Part I, it was shown that tropical moisture within the AR contributed 50–60% of the moisture above the 4 km level, which corresponded to the height of the 0°C isotherm as the AR emerged over the Southern Ocean at Tasmania and that at altitudes below the 0°C isotherm, moisture was largely of midlatitude origin. This paper analyzed the microphysical processes within the tropical-sourced and midlatitude-sourced layers within the AR. The AR originated from northwest Australia at 10°S and moved southeastward over Tasmania, Australia, where the NSF/NCAR G-V aircraft made two passes through the AR during its departure from and return to Hobart airport. Measurements of reflectivity Z_e and vertical radial velocity V_r from the airborne, nadir-directed HIAPER cloud radar provided detailed information on the fine-scale features of the prefrontal and frontal precipitation bands associated with the AR while a suite of microphysical instruments provided measurements of the concentration, size, and morphological properties of liquid- and ice-phase particles and PSDs spanning from 1 μm to 3.2 mm.

The analyses presented here represent the first study detailing the microphysical evolution of precipitation within a Southern Hemisphere AR. Moreover, the collocation of radar and microphysical data offers a rare perspective of the relationship between the microphysical properties of number concentration, particle size, and habit and the precipitation structure of an AR, information rarely available from previous AR field experiments.

The following are the major findings of this study:

1. The two rainbands composing the AR were primarily stratiform in character, with distinct radar bright bands. Weak embedded convection may have been present at middle altitudes of the prefrontal band, but deep convection was not observed.
2. The clouds composing the AR were deep, with tops at 10–12 km and cloud top temperatures near −50°C. The upper part of the cloud sampled at −20°C was devoid of supercooled water. The habits of ice particles falling through the clouds were typical of low temperatures (primarily irregular assemblages of plates and columns). INP concentrations were 0.01–0.04 L^{-1} at $T = -20$°C based on continuous flow diffusion chamber and ice spectrometer measurements. The INP concentrations were much lower than the peak ice particle concentrations of 100–400 L^{-1} and more typical ice particle concentrations of 10–20 L^{-1} observed at −20°C.
3. Ice particle concentrations at −12°C typically were of the order 1–10 L^{-1} with peaks near 30 L^{-1}, while INP concentrations at the warmest temperature sampled (−16.5°C) were 0.006 L^{-1}. At −16°C, supercooled water was present, riming was evident, some dendritic particles were observed, and some aggregation of particles occurred at that level.
4. At lower altitudes between temperatures of −8°C and −4°C, an order of magnitude increase in ice particle concentrations and the appearance of columnar habits was observed. Although required conditions for the Hallett-Mossop mechanism were not present at the aircraft location between −8°C and −6°C, they were between −6°C and −4°C. The microphysical evidence, together with attenuation of the radar signal (providing evidence of supercooled water presence below the aircraft altitude), was consistent with the Hallett-Mossop mechanism as the source of the increase in particle concentrations.
5. Ice particles falling though the 0°C level and melting provided the "seeds" from which subsequent growth by collision-coalescence occurred in the midlatitude-sourced moisture region below the altitude of the 0°C isotherm. In this region, raindrops grew to sizes of 3 mm, and precipitation rates averaged 16 mm hr^{-1}.

While many studies have analyzed the seeder-feeder mechanism with respect to the influence of orographic lift within East Pacific ARs (e.g., Kingsmill et al., 2016; White et al., 2003, 2015), European ARs (Browning, 2018), and South American ARs (Viale et al., 2013), this study together with Part I demonstrates that high-level tropical-sourced moisture lofted in tropical weather systems and lower altitude midlatitude-sourced moisture associated with frontal-scale ascent can act together from a microphysical perspective in a seeder-feeder type process to produce precipitation in atmospheric river flows.

Data Availability Statement

The data that support the findings of this study can be obtained at the following addresses: CFDC INP data (https://data.eol.ucar.edu/dataset/552.044), IS INP data (https://data.eol.ucar.edu/dataset/552.045), 2D-S size distributions (https://doi.org/10.26023/8HMG-WQP3-XA0X), PHIPS stereo imaging data (https://doi.org/10.5065/D62B8WWF), PHIPS single particle data (i.e., scattering angle info) (https://doi.org/10.5065/D6639NKQ), Flight-level data (e.g., RICE, KWC, navigation data) (https://doi.org/10.5065/D6M32TM9), HCR radar time series data (https://doi.org/10.5065/D6D7998S), NASA SatCORPS Himawari Cloud Retrieval Data (https://doi.org/10.5065/D6CC0ZFJ), and GPM-DPR data (https://doi.org/10.5067/GPM/DPR/GPM/2A/05).

References

Abdelmonem, A., Järvinen, E., Duft, D., Hirst, E., Vogt, S., Leisner, T., & Schnaiter, M. (2016). PHIPS–HALO: The airborne Particle Habit Imaging and Polar Scattering probe. Part 1: Design and operation. *Atmospheric Measurement Techniques*, *9*(7), 3131–3144. https://doi.org/10.5194/amt-9-3131-2016

Bailey, M. P., & Hallett, J. (2009). A comprehensive habit diagram for atmospheric ice crystals: Confirmation from the laboratory, AIRS II, and other field studies. *Journal of the Atmospheric Sciences*, *66*(9), 2888–2899. https://doi.org/10.1175/2009JAS2883.1

Baumgardner, D., & Korolev, A. (1997). Airspeed corrections for optical array probe sample volumes. *Journal of Atmospheric and Oceanic Technology*, *14*(5), 1224–1229. https://doi.org/10.1175/1520-0426(1997)014<1224:ACFOAP>2.0.CO;2

Baumgardner, D., & Rodi, A. (1989). Laboratory and wind tunnel evaluations of the Rosemount icing detector. *Journal of Atmospheric and Oceanic Technology*, *6*(6), 971–979. https://doi.org/10.1175/1520-0426(1989)006<0971:LAWTEO>2.0.CO;2

Bergeron, T. (1965). On the Low-Level Redistribution of Atmospheric Water Caused by Orography. Paper presented at Proc. Int. Conf. on Cloud Physics, IAMAP/WMO, Tokyo, Japan, 96–100.

Biter, C. J., Dye, J. E., Huffman, D., & King, W. D. (1987). The drop-size response of the CSIRO liquid water probe. *Journal of Atmospheric and Oceanic Technology*, *4*(3), 359–367. https://doi.org/10.1175/1520-0426(1987)004<0359:TDSROT>2.0.CO;2

Bradley, S. G., & King, W. D. (1979). Frequency response of the CSIRO liquid water probe. *Journal of Applied Meteorology*, *18*, 361–366. https://doi.org/10.1175/1520-0450(1979)018<0361:FROTCL>2.0.CO;2

Browning, K. (2018). Atmospheric rivers in the U.K. *Bulletin of the American Meteorological Society*, *99*(6), 1108–1109. https://doi.org/10.1175/BAMS-D-17-0291.1

Browning, K. A., & Pardoe, C. W. (1973). Structure of low-level jet streams ahead of midlatitude cold fronts. *Quarterly Journal of the Royal Meteorological Society*, *99*(422), 619–638. https://doi.org/10.1002/qj.49709942204

Cannon, F., Ralph, F. M., Wilson, A. M., & Lettenmaier, D. P. (2017). GPM satellite radar measurements of precipitation and freezing level in atmospheric rivers: Comparison with ground-based radars and reanalyses. *Journal of Geophysical Research: Atmospheres*, *122*, 12,747–12,764. https://doi.org/10.1002/2017JD027355

Choularton, T. W., Griggs, D. J., Humood, B. Y., & Latham, J. (1980). Laboratory studies of riming, and its relation to ice splinter production. *Quarterly Journal of the Royal Meteorological Society*, *106*(448), 367–374. https://doi.org/10.1002/qj.49710644809

Choularton, T. W., Latham, J., & Mason, B. J. (1978). A possible mechanism of ice splinter production during riming. *Nature*, *274*(5673). https://doi.org/10.1038/274791a0

Cober, S. G., Isaac, G. A., Korolev, A. V., & Strapp, J. W. (2001). Assessing cloud-phase conditions. *Journal of Applied Meteorology*, *40*(11), 1967–1983. https://doi.org/10.1175/1520-0450(2001)040<1967:ACPC>2.0.CO;2

De Mott, P. J., Hill, T. C. J., Petters, M. D., Bertram, A. K., Tobo, Y., Mason, R. H., et al. (2017). Comparative measurements of ambient atmospheric concentrations of ice nucleating particles using multiple immersion freezing methods and a continuous flow diffusion chamber. *Atmospheric Chemistry and Physics*, *17*, 11,227–11,245. https://doi.org/10.5194/acp-17-11227-2017

Dettinger, M. D., Ralph, F. M., Das, T., Neiman, P. J., & Cayan, D. R. (2011). Atmospheric rivers, floods and the water resources of California. *Watermark*, *3*(4), 445–478. https://doi.org/10.3390/w3020445

Ellis, S., Loew, E., Burghart, C., Tsai, P., Dixon, M., Vivekanandan, J., & Lee, W. C. (2017). Use of the Earth's surface as a reference to correct airborne radar radial velocity measurements for platform motion. In 38th Conference on Radar Meteorology. Chicago, IL: Amer. Meteor. Soc.. Retrieved from https://ams.confex.com/ams/38RADAR/webprogram/Paper321171.html

Field, P. R. (1999). Aircraft observations of ice crystal evolution in an altostratus cloud. *Journal of the Atmospheric Sciences*, *56*(12), 1925–1941. https://doi.org/10.1175/1520-0469(1999)056<1925:AOOICE>2.0.CO;2

Field, P. R., Heymsfield, A. J., & Bansemer, A. (2006). Shattering and particle interarrival times measured by optical array probes in ice clouds. *Journal of Atmospheric and Oceanic Technology*, *23*(10), 1357–1371. https://doi.org/10.1175/JTECH1922.1

Field, P. R., Wood, R., Brown, P. R. A., Kaye, P. H., Hirst, E., Greenaway, R., & Smith, J. A. (2003). Ice particle interarrival times measured with a fast FSSP. *Journal of Atmospheric and Oceanic Technology*, *20*(2), 249–261. https://doi.org/10.1175/1520-0426(2003)020<0249:IPITMW>2.0.CO;2

Finlon, J. A., McFarquhar, G. M., Nesbitt, S. W., Rauber, R. M., Morrison, H., Wu, W., & Zhang, P. (2019). A novel approach for characterizing the variability in mass–dimension relationships: Results from MC3E. *Atmospheric Chemistry and Physics*, *19*(6), 3621–3643. https://doi.org/10.5194/acp-19-3621-2019

Griggs, D. J., & Choularton, T. W. (1983). Freezing modes of riming droplets with application to ice splinter production. *Quarterly Journal of the Royal Meteorological Society*, *109*(459), 243–253. https://doi.org/10.1002/qj.49710945912

Hallett, J., & Mossop, S. C. (1974). Production of secondary ice particles during the riming process. *Nature*, *249*(5452), 26–28. https://doi.org/10.1038/249026a0

Heymsfield, A. J., & Baumgardner, D. (1985). Summary of a workshop on processing 2D probe data. *Bulletin of the American Meteorological Society*, *66*(4), 437–440. https://doi.org/10.1175/1520-0477-66.4.437

Holroyd, E. W. (1987). Some techniques and uses of 2D-C habit classification software for snow particles. *Journal of Atmospheric and Oceanic Technology*, *4*(3), 498–511. https://doi.org/10.1175/1520-0426(1987)004<0498:STAUOC>2.0.CO;2

Hou, A. Y., Kakar, R. K., Neeck, S., Azarbarzin, A. A., Kummerow, C. D., Kojima, M., et al. (2014). The global precipitation measurement mission. *Bulletin of the American Meteorological Society*, *95*(5), 701–722. https://doi.org/10.1175/BAMS-D-13-00164.1

International Telecommunication Union (2013). Attenuation by atmospheric gases (Recommendation ITU-R P.676–10). Radiocommunication Sector of International Telecommunication Union. Retrieved from https://www.itu.int/dms_pubrec/itu-r/rec/p/R-REC-P.676-10-201309-S!!PDF-E.pdf (Retrieved March 25, 2019)

Jackson, R. C., McFarquhar, G. M., Korolev, A. D., Earle, M. E., Liu, P. S. K., & Lawson, R. P. (2012). The dependence of ice microphysics on aerosol concentrations in arctic mixed-phased stratus clouds during ISDAC and M-PACE. *Journal of Geophysical Research*, *117*, D15207. https://doi.org/10.1029/2012JD017668

Jackson, R. C., McFarquhar, G. M., Stith, J., Beals, M., Shaw, R. A., Jensen, J., & Korolev, A. (2014). An assessment of the impact of anti-shattering tips and artifact removal techniques on cloud ice size distributions measured by the 2D cloud probe. *Journal of Atmospheric and Oceanic Technology*, *31*(12), 2567–2590. https://doi.org/10.1175/JTECH-D-13-00239.1

King, W. D., Parkin, D. A., & Handsworth, R. J. (1978). A hot-wire liquid water device having fully calculable response characteristics. *Journal of Applied Meteorology*, *17*, 1809–1813. https://doi.org/10.1175/1520-0450(1978)017<1809:AHWLWD>2.0.CO;2

Kingsmill, D. E., Neiman, P. J., Ralph, F. M., & White, A. B. (2006). Synoptic and topographic variability of northern California precipitation characteristics in landfalling winter storms observed during CALJET. *Monthly Weather Review*, *134*(8), 2072–2094. https://doi.org/10.1175/MWR3166.1

Kingsmill, D. E., Neiman, P. J., & White, A. B. (2016). Microphysics regime impacts on the relationship between orographic rain and orographic forcing in the coastal mountains of northern California. *Journal of Hydrometeorology*, *17*(11), 2905–2922. https://doi.org/10.1175/JHM-D-16-0103.1

Korolev, A., Emery, E., & Creelman, K. (2013). Modification and tests of particle probe tips to mitigate effects of ice shattering. *Journal of Atmospheric and Oceanic Technology*, *30*(4), 690–708. https://doi.org/10.1175/JTECH-D-12-00142.1

Korolev, A. V., Emery, E. F., Strapp, J. W., Cober, S. G., Isaac, G. A., Wasey, M., & Marcotte, D. (2011). Small ice particles in tropospheric clouds: Fact or artifact? Airborne icing instrumentation evaluation experiment. *Bulletin of the American Meteorological Society*, *92*(8), 967–973. https://doi.org/10.1175/2010BAMS3141.1

Lance, S. (2012). Coincidence Errors in a Cloud Droplet Probe (CDP) and a Cloud and Aerosol Spectrometer (CAS), and the Improved Performance of a Modified CDP. *Journal of Atmospheric and Oceanic Technology*, *29*(10), 1532–1541. https://doi.org/10.1175/JTECH-D-11-00208.1

Lance, S., Brock, C. A., Rogers, D., & Gordon, J. A. (2010). Water droplet calibration of the cloud droplet probe (CDP) and in-flight performance in liquid, ice and mixed-phase clouds during ARCPAC. *Atmospheric Measurement Techniques*, *3*, 1683–1706. https://doi.org/10.5194/amt-3-1683-2010

Lavers, D. A., & Villarini, G. (2013). Atmospheric rivers and flooding over the Central United States. *Journal of Climate*, *26*(20), 7829–7836. https://doi.org/10.1175/JCLI-D-13-00212.1

Leung, L. R., & Qian, Y. (2009). Atmospheric rivers induced heavy precipitation and flooding in the western U.S. simulated by the WRF regional climate model. *Geophysical Research Letters*, *36*, L03820. https://doi.org/10.1029/2008GL036445

Levin, E. J. T., DeMott, P. J., Suski, K. J., Boose, Y., Hill, T. C. J., McCluskey, C. S., et al. (2019). Characteristics of ice nucleating particles in and around California winter storms. *Journal of Geophysical Research: Atmospheres*, *124*, 11,530–11,551. https://doi.org/10.1029/2019JD030831

Li, L., Heymsfield, G. M., Tian, L., & Racette, P. E. (2005). Measurements of ocean surface backscattering using an airborne 94-GHz cloud radar—Implication for calibration of airborne and spaceborne W-band radars. *Journal of Atmospheric and Oceanic Technology*, *22*(7), 1033–1045. https://doi.org/10.1175/JTECH1722.1

Liebe, H. J. (1985). An updated model for millimeter wave propagation in moist air. *Radio Science*, *20*(5), 1069–1089. https://doi.org/10.1029/RS020i005p01069

Locatelli, J. D., & Hobbs, P. V. (1974). Fall speeds and masses of solid precipitation particles. *Journal of Geophysical Research*, *79*(15), 2185–2197. https://doi.org/10.1029/JC079i015p02185

Ma, Z., Kuo, Y.-H., Ralph, F. M., Neiman, P. J., Wick, G. A., Sukovich, E., & Wang, B. (2011). Assimilation of GPS radio occultation data for an intense atmospheric river with the NCEP regional GSI system. *Monthly Weather Review*, *139*(7), 2170–2183. https://doi.org/10.1175/2011MWR3342.1

Martner, B. E., Yuter, S. E., White, A. B., Matrosov, S. Y., Kingsmill, D. E., & Ralph, F. M. (2008). Raindrop size distributions and rain characteristics in California coastal rainfall for periods with and without a radar bright band. *Journal of Hydrometeorology*, *9*(3), 408–425. https://doi.org/10.1175/2007JHM924.1

Matrosov, S. Y. (2012). Observations of wintertime U.S. West Coast precipitating systems with W-band satellite radar and other spaceborne instruments. *Journal of Hydrometeorology*, *13*(1), 223–238. https://doi.org/10.1175/JHM-D-10-05025.1

Matrosov, S. Y. (2013). Characteristics of landfalling atmospheric rivers inferred from satellite observations over the eastern North Pacific Ocean. *Monthly Weather Review*, *141*(11), 3757–3768. https://doi.org/10.1175/MWR-D-12-00324.1

Matrosov, S. Y., Cifelli, R., Neiman, P. J., & White, A. B. (2016). Radar rain-rate estimators and their variability due to rainfall type: An assessment based on hydrometeorology testbed data from the Southeastern United States. *Journal of Applied Meteorology and Climatology*, *55*(6), 1345–1358. https://doi.org/10.1175/JAMC-D-15-0284.1

McFarquhar, G. M., Finlon, J. A., Stechman, D. M., Wu, W., Jackson, R. C., & Freer, M. (2018). University of Illinois/Oklahoma optical array probe (OAP) processing software. https://doi.org/10.5281/ZENODO.1285969 (Accessed 5 January 2020)

Minnis, P., Nguyen, L., Palikonda, R., Heck, P. W., Spangenberg, D. A., Doelling, D. R., Szedung, S.-M. (2008). Near-real time cloud retrievals from operational and research meteorological satellites. In SPIE Remote Sensing of Clouds and the Atmosphere XIII (Vol. 7107, p. 710703). International Society for Optics and Photonics. https://doi.org/10.1117/12.800344

Minnis, P., Sun-Mack, S., Young, D. F., Heck, P. W., Garber, D. P., Chen, Y., & Yang, P. (2011). CERES edition-2 cloud property retrievals using TRMM VIRS and Terra and Aqua MODIS data—Part I: Algorithms. *IEEE Transactions on Geoscience and Remote Sensing*, *49*(11), 4374–4400. https://doi.org/10.1109/TGRS.2011.2144601

Moore, B. J., Neiman, P. J., Ralph, F. M., & Barthold, F. E. (2012). Physical processes associated with heavy flooding rainfall in Nashville, Tennessee, and vicinity during 12 May 2010: The role of an atmospheric river and mesoscale convective systems. *Monthly Weather Review*, *140*(2), 358–378. https://doi.org/10.1175/MWR-D-11-00126.1

Mossop, S. C., & Hallett, J. (1974). Ice crystal concentration in cumulus clouds: Influence of the drop Spectrum. *Science*, *186*(4164), 632–634. https://doi.org/10.1126/science.186.4164.632

Nakamura, J., Lall, U., Kushnir, Y., Robertson, A. W., & Seager, R. (2013). Dynamical structure of extreme floods in the U.S. Midwest and the United Kingdom. *Journal of Hydrometeorology*, *14*(2), 485–504. https://doi.org/10.1175/JHM-D-12-059.1

Neiman, P. J., Gaggini, N., Fairall, C. W., Aikins, J., Spackman, J. R., Leung, L. R., & White, A. B. (2017). An analysis of coordinated observations from NOAA's Ronald H. Brown ship and G-IV aircraft in a landfalling atmospheric river over the North Pacific during CalWater-2015. *Monthly Weather Review*, *145*(9), 3647–3669. https://doi.org/10.1175/MWR-D-17-0055.1

Neiman, P. J., Moore, B. J., White, A. B., Wick, G. A., Aikins, J., Jackson, D. L., & Ralph, F. M. (2016). An airborne and ground-based study of a long-lived and intense atmospheric river with mesoscale frontal waves impacting California during CalWater-2014. *Monthly Weather Review*, *144*(3), 1115–1144. https://doi.org/10.1175/MWR-D-15-0319.1

Neiman, P. J., Ralph, F. M., Wick, G. A., Kuo, Y.-H., Wee, T.-K., Ma, Z., & Dettinger, M. D. (2008). Diagnosis of an intense atmospheric river impacting the Pacific Northwest: Storm summary and offshore vertical structure observed with COSMIC satellite retrievals. *Monthly Weather Review*, *136*(11), 4398–4420. https://doi.org/10.1175/2008MWR2550.1

Neiman, P. J., Ralph, F. M., Wick, G. A., Lundquist, J. D., & Dettinger, M. D. (2008). Meteorological characteristics and overland precipitation impacts of atmospheric rivers affecting the West Coast of North America based on eight years of SSM/I satellite observations. *Journal of Hydrometeorology*, *9*(1), 22–47. https://doi.org/10.1175/2007JHM855.1

Pfahl, S., Madonna, E., Boettcher, M., Joos, H., & Wernli, H. (2014). Warm conveyor belts in the ERA-Interim dataset (1979–2010). Part II: Moisture origin and relevance for precipitation. *Journal of Climate*, *27*(1), 27–40. https://doi.org/10.1175/JCLI-D-13-00223.1

Protat, A., & Williams, C. R. (2011). The accuracy of radar estimates of ice terminal fall speed from vertically pointing Doppler radar measurements. *Journal of Applied Meteorology and Climatology*, *50*, 2120–2138. https://doi.org/10.1175/JAMC-D-10-05031.1

Ralph, F. M., Dettinger, M. C. L., Cairns, M. M., Galarneau, T. J., & Eylander, J. (2018). Defining "atmospheric river": How the glossary of meteorology helped resolve a debate. *Bulletin of the American Meteorological Society*, *99*(4), 837–839. https://doi.org/10.1175/BAMS-D-17-0157.1

Ralph, F. M., Iacobellis, S. F., Neiman, P. J., Cordeira, J. M., Spackman, J. R., Waliser, D. E., & Fairall, C. (2017). Dropsonde observations of total integrated water vapor transport within North Pacific atmospheric rivers. *Journal of Hydrometeorology*, *18*(9), 2577–2596. https://doi.org/10.1175/JHM-D-17-0036.1

Ralph, F. M., Neiman, P. J., & Rotunno, R. (2005). Dropsonde observations in low-level jets over the Northeastern Pacific Ocean from CALJET-1998 and PACJET-2001: Mean vertical-profile and atmospheric-river characteristics. *Monthly Weather Review*, *133*(4), 889–910. https://doi.org/10.1175/MWR2896.1

Ralph, F. M., Neiman, P. J., & Wick, G. A. (2004). Satellite and CALJET aircraft observations of atmospheric rivers over the eastern North Pacific Ocean during the winter of 1997/98. *Monthly Weather Review*, *132*(7), 1721–1745. https://doi.org/10.1175/1520-0493(2004)132<1721:SACAOO>2.0.CO;2

Ralph, F. M., Neiman, P. J., Wick, G. A., Gutman, S. I., Dettinger, M. D., Cayan, D. R., & White, A. B. (2006). Flooding on California's Russian River: Role of atmospheric rivers. *Geophysical Research Letters*, *33*, L13801. https://doi.org/10.1029/2006GL026689

Rauber, R. M., Ellis, S. M., Vivekanandan, J., Stith, J., Lee, W. C., McFarquhar, G. M., & Janiszeski, A. (2017). Finescale structure of a snowstorm over the northeastern United States: A first look at high-resolution HIAPER cloud radar observations. *Bulletin of the American Meteorological Society*, *98*(2), 253–269. https://doi.org/10.1175/BAMS-D-15-00180.1

Rauber, R. M., Hu, H., Dominguez, F., Nesbitt, S. W., McFarquhar, G. M., Zaremba, T., & Finlon, J. A. (2020). Structure of an atmospheric river over Australia and the Southern Ocean. Part I: Tropical and mid-latitude water vapor fluxes as a seeder-feeder process. *Journal of Geophysical Research: Atmospheres*, *125*, e2020JD032513. https://doi.org/10.1029/2020JD032513

Rosenow, A., Rauber, R. M., McFarquhar, G. M., Jewett, B. F., Plummer, D., & Leon, D. (2014). Vertical velocity and physical structure of generating cells and elevated convection in the comma-head region of continental winter cyclones. *Journal of the Atmospheric Sciences*, *71*(5), 1538–1558. https://doi.org/10.1175/JAS-D-13-0249.1

Rutz, J. J., Steenburgh, W. J., & Ralph, F. M. (2014). Climatological characteristics of atmospheric rivers and their inland penetration over the Western United States. *Monthly Weather Review*, *142*(2), 905–921. https://doi.org/10.1175/MWR-D-13-00168.1

Schnaiter, M., Järvinen, E., Abdelmonem, A., & Leisner, T. (2018). PHIPS-HALO: The airborne particle habit imaging and polar scattering probe – Part 2: Characterization and first results. *Atmospheric Measurement Techniques*, *11*(1), 341–357. https://doi.org/10.5194/amt-11-341-2018

Smith, W., & Minnis, P. (2018). NASA SatCORPS Himawari cloud retrieval data. Version 2.1. UCAR/NCAR - earth observing laboratory. https://doi.org/10.5065/D6CC0ZFJ. Accessed 26 Jan 2020.

Stith, J. L., Ramanathan, V., Cooper, W. A., Roberts, G., DeMott, P. J., Carmichael, G., et al. (2009). An overview of aircraft observations from the Pacific Dust Experiment campaign. *Journal of Geophysical Research*, *114*, D05207. https://doi.org/10.1029/2008JD010924

UCAR/NCAR – Earth Observing Laboratory (2014). HIAPER cloud radar (HCR) (Tech. Rep.). UCAR/NCAR – Earth Observing Laboratory. https://doi.org/10.5065/D6BP00TP

UCAR/NCAR – Earth Observing Laboratory (2018a). SOCRATES HCR noise source calibration. UCAR/NCAR – Earth Observing Laboratory. Retrieved from https://www.eol.ucar.edu/node/14065 (Retrieved March 25, 2019)

UCAR/NCAR – Earth Observing Laboratory (2018b). SOCRATES HCR ocean scan calibration. UCAR/NCAR – Earth Observing Laboratory. Retrieved from https://www.eol.ucar.edu/node/14066 (Retrieved March 25, 2019)

Viale, M., Houze, R. A., & Rasmussen, K. L. (2013). Upstream orographic enhancement of a narrow cold-frontal rainband approaching the Andes. *Monthly Weather Review*, *141*(5), 1708–1730. https://doi.org/10.1175/MWR-D-12-00138.1

Waliser, D., & Guan, B. (2017). Extreme winds and precipitation during landfall of atmospheric rivers. *Nature Geoscience*, *10*(3), 179–183. https://doi.org/10.1038/ngeo2894

White, A. B., Neiman, P. J., Creamean, J. M., Coleman, T., Ralph, F. M., Prather, K. A., & Prather, K. A. (2015). The impacts of California's San Francisco Bay area gap on precipitation observed in the Sierra Nevada during HMT and CalWater. *Journal of Hydrometeorology*, *16*(3), 1048–1069. https://doi.org/10.1175/JHM-D-14-0160.1

White, A. B., Neiman, P. J., Ralph, F. M., Kingsmill, D. E., & Persson, P. O. G. (2003). Coastal orographic rainfall processes observed by radar during the California Land-Falling Jets Experiment. *Journal of Hydrometeorology*, *4*(2), 264–282. https://doi.org/10.1175/1525-7541(2003)4<264:CORPOB>2.0.CO;2

Wick, G. A., Neiman, P. J., & Ralph, F. M. (2013). Description and validation of an automated objective technique for identification and characterization of the integrated water vapor signature of atmospheric rivers. *IEEE Geoscience and Remote Sensing Society*, *51*(4), 2166–2176. https://doi.org/10.1109/TGRS.2012.2211024

Wu, W., & McFarquhar, G.M. (2019). NSF/NCAR GV HIAPER fast 2DS particle size distribution (PSD) product data. Version 1.1. UCAR/NCAR – Earth observing laboratory. https://doi.org/10.26023/e95a-fkyf-7p0r, accessed on 06 June 2020.

Yuter, S. E., & Houze, R. A. (1995). Three-dimensional kinematic and microphysical evolution of Florida cumulonimbus. Part I: Spatial distribution of updrafts, downdrafts, and precipitation. *Monthly Weather Review*, *123*(7), 1921–1940. https://doi.org/10.1175/1520-0493(1995)123<1921:Tdkame>2.0.Co;2

Zagrodnik, J. P., McMurdie, L. A., & Houze, R. A. (2018). Stratiform precipitation processes in cyclones passing over a coastal mountain range. *Journal of the Atmospheric Sciences*, *75*(3), 983–1004. https://doi.org/10.1175/JAS-D-17-0168.1

Zhu, Y., & Newell, R. E. (1998). A proposed algorithm for moisture fluxes from atmospheric rivers. *Monthly Weather Review*, *126*(3), 725–735. https://doi.org/10.1175/1520-0493(1998)126<0725:APAFMF>2.0.CO;2